Available online at www.sciencedirect.com
ScienceDirect
Icarus 195 (2008) 184–205
ICARUS
www.elsevier.com/locate/icarus

A radar survey of M- and X-class asteroids

Michael K. Shepard [a,*], Beth Ellen Clark [b], Michael C. Nolan [c], Ellen S. Howell [c], Christopher Magri [d], Jon D. Giorgini [e], Lance A.M. Benner [e], Steven J. Ostro [e], Alan W. Harris [f], Brian Warner [g], Donald Pray [h], Petr Pravec [i], Michael Fauerbach [j], Thomas Bennett [j], Alain Klotz [k], Raoul Behrend [l], Horacio Correia [k], Josep Coloma [m], Silvano Casulli [n], Andrew Rivkin [o]

[a] *Department of Geography and Geosciences, Bloomsburg University of Pennsylvania, 400 E. Second St., Bloomsburg, PA 17815, USA*
[b] *Ithaca College, Ithaca, NY 14853, USA*
[c] *NAIC/Arecibo Observatory, HC 3 Box 53995, Arecibo, PR 00612, USA*
[d] *University of Maine at Farmington, Farmington, ME 04938, USA*
[e] *Jet Propulsion Laboratory, Pasadena, CA 91109, USA*
[f] *Space Science Institute, La Canada, CA 91011-3364, USA*
[g] *Palmer Divide Observatory/Space Science Institute, Colorado Springs, CO, USA*
[h] *Carbuncle Hill Observatory, Greene, RI, USA*
[i] *Astronomical Institute, Academy of Sciences of the Czech Republic, Ondrejov, CZ-25165, Czech Republic*
[j] *Florida Gulf Coast University, Ft. Meyers, FL 33965, USA*
[k] *TAROT, Haute-Provence Observatory, St.-Michel l'Observatoire, France*
[l] *TAROT, Centre d'Astronomie de St.-Michel l'Observatoire, France*
[m] *Agrupacion Astronomica de Sabadell, Sabadell, Barcelona, Spain*
[n] *Osservatorio Astronomico Vallemare di Borbona, Rome, Italy*
[o] *Johns Hopkins Applied Physics Laboratory, Laurel, MD 20723, USA*

Received 16 May 2007; revised 9 November 2007

Available online 18 January 2008

Abstract

We observed ten M- and X-class main-belt asteroids with the Arecibo Observatory's S-band (12.6 cm) radar. The X-class asteroids were targeted based on their albedos or other properties which suggested they might be M-class. This work brings the total number of main-belt M-class asteroids observed with radar to 14. We find that three of these asteroids have rotation rates significantly different from what was previously reported. Based on their high radar albedo, we find that only four of the fourteen—16 Psyche, 216 Kleopatra, 758 Mancunia, and 785 Zwetana—are almost certainly metallic. 129 Antigone has a moderately high radar albedo and we suggest it may be a CH/CB/Bencubbinite parent body. Three other asteroids, 97 Klotho, 224 Oceana, and 796 Sarita have radar albedos significantly higher than the average main belt asteroid and we cannot rule out a significant metal content for them. Five of our target asteroids, 16 Psyche, 129 Antigone, 135 Hertha, 758 Mancunia, and 785 Zwetana, show variations in their radar albedo with rotation. We can rule out shape and composition in most cases, leaving variations in thickness, porosity, or surface roughness of the regolith to be the most likely causes. With the exception of 129 Antigone, we find no hydrated M-class asteroids (W-class; Rivkin, A.S., Howell, E.S., Lebofsky, L.A., Clark, B.E., Britt, D.T., 2000. Icarus 145, 351–368) to have high radar albedos.

Keywords: Asteroids; Asteroids, composition; Surfaces, asteroids

1. Introduction

The Tholen (1984) M- and X-asteroid classes are most enigmatic. X-class asteroids are defined by featureless spectra with red slopes and an unknown visual albedo. Asteroids with these spectral characteristics and visual albedos of 0.10–0.30 are clas-

* Corresponding author. Fax: +1 570 389 3028.
E-mail address: mshepard@bloomu.edu (M.K. Shepard).

0019-1035/$ – see front matter
doi:10.1016/j.icarus.2007.11.032

sified as M; those with lower albedos are classified as P, and those with higher albedos are classified as E. In this paper, we focus exclusively on M- or X-class objects with visual albedos consistent with an M classification. In a companion paper (Shepard et al., 2008) we describe radar observations of two E-class main-belt asteroids.

Historically, M-class asteroids were thought to be the denuded metallic cores of disrupted parent bodies or possibly enstatite chondrites (Gaffey, 1976; Bell et al., 1989; Cloutis et al., 1990) but this paradigm has changed significantly in the past few years. Several workers have discovered subtle spectral features evident in both X- and M-class asteroids, some of which are inconsistent with metallic compositions (Hardersen et al., 2002; Clark et al., 2004). Others have discovered evidence of hydration features, also considered to be inconsistent with the metallic core or enstatite chondrite interpretation (Jones et al., 1990; Rivkin et al., 1995, 2000). At least one, 22 Kalliope, is binary, and its bulk density of 2.4 $\mathrm{g\,cm^{-3}}$ is not consistent with a denuded core (Margot and Brown, 2003). In short, it has become evident that M-class asteroids are an amalgam of different compositions. At present, viable candidate analogs include: pure NiFe metal, iron meteorites with significant low Fe-silicates, enstatite chondrites, CH/CB/bencubbinites, and carbonaceous chondrites (Bell et al., 1989; Gaffey, 1976; Cloutis et al., 1990; Gaffey et al., 1993; Vilas, 1994; Hardersen et al., 2002). The first three of these would not be expected to contain hydrated phases; the latter two may.

Spectral analysis by itself is insufficient to determine which M-asteroids are metallic because all of these compositions have only subtle or similarly featureless spectra. Radar, however, is a better tool for identifying metallic compositions. Because iron is several times denser than rock-forming silicates, an asteroid composed primarily of iron will have a significantly higher radar reflectivity than one composed of silicates. The major difficulty with using radar to probe the main-belt asteroids (MBAs) has been radar system sensitivity: echo strength falls off as the fourth power of distance. Until 1998, only a few of the larger M-class asteroids were detectable from Arecibo Observatory, the largest radar facility on Earth. The 1998 upgrade in transmitter power and receiver sensitivity (Campbell et al., 1997; Nolan et al., 1998) has extended the capability of Arecibo so that dozens of M-class asteroids are now within reach.

Until our survey began in 2004, only seven M-class MBAs had been detected (Table 1). Of those, only two—16 Psyche and 216 Kleopatra—were observed to have radar albedos consistent with metallic surfaces. 216 Kleopatra has the largest radar albedo of any MBA, 0.6 ± 0.1 (Ostro et al., 2000). 16 Psyche's radar albedo is estimated to be considerably lower, ~0.31, but is still consistent with a moderately porous metallic regolith (Ostro et al., 1985). The rest have radar albedos similar to other MBAs and, with the possible exception of 796 Sarita, are inconsistent with largely metallic surfaces of any reasonable porosity.

For our survey, we identified all XM-class targets that could be detected over the next 25 years at Arecibo if a radar albedo of at least 0.1 is assumed. Even if just detected, we can estimate an asteroid's radar albedo and make an estimate of its bulk density and metal content. Higher signal-to-noise ratios (SNRs) are desirable to look for rotationally dependent properties and, in a few exceptional cases, to allow for delay–Doppler imaging. Where possible, we enlisted the NASA Infrared Telescope Facility (IRTF) to complement the radar observations. Those results are in a companion paper by Ockert-Bell et al. (2008). Additional lightcurve observations of several of these asteroids were made by co-authors in support of the radar work. Their specific contributions are noted by using their initials.

Table 1
M-class asteroids observed by radar prior to 2004

Asteroid	$\hat{\sigma}_{OC}$	μ_c	Class	Reference
16 Psyche	0.31 ± 0.08	0.17 ± 0.05	M	a,b
21 Lutetia	0.19 ± 0.07	0.22 ± 0.07	W	b
22 Kalliope	0.15 ± 0.05	0.07 ± 0.10	W	b,c
83 Beatrix	0.073 ± 0.026	0.23 ± 0.11		d
97 Klotho	0.21 ± 0.05	0.23 ± 0.07		b
216 Kleopatra	0.60 ± 0.15	0.00 ± 0.04	M	e
796 Sarita	0.25 ± 0.10	–	M	b

$\hat{\sigma}_{OC}$ is OC radar albedo and μ_c is the polarization ratio. Class is M (Tholen, 1984) or W for M-class asteroids on which a 3 μm absorption feature has been detected (Rivkin et al., 1995, 2000).
[a] Ostro et al. (1985).
[b] Magri et al. (1999).
[c] Margot and Brown (2003).
[d] Magri et al. (2007a).
[e] Ostro et al. (2000).

2. Background

For all our targets, we initially assume them to be ellipsoids with axes $a \geqslant b \geqslant c$, and the c-axis is the rotation axis. In the remainder of this section, we briefly review the other conventions and equations used in this paper.

2.1. Optical analysis

To place constraints on a target's diameter, we use the relationship between visual albedo (p_v), effective diameter (D_{eff}, in km) and absolute magnitude (H) derived by Pravec and Harris (2007):

$$\log p_v = 6.247 - 2 \log D_{\mathrm{eff}} - 0.4H. \quad (1)$$

The effective diameter D_{eff} is the diameter of a sphere with the same projected area as the asteroid.

2.2. Radar analysis

Our observational, reduction, and analysis techniques are similar to those described by Mitchell et al. (1996), Ostro et al. (2000), and Magri et al. (2007a). Each observing cycle or "run" consisted of transmission of a circularly polarized, 2380 MHz (12.6 cm) signal for the round-trip light travel time to the target, followed by reception of echoes for a similar duration in the opposite (OC) and same (SC) senses of polarization as transmitted. We operated in two modes: "continuous wave" (CW), where we measure the spectrum of the Doppler

shift of the reflected radio waves, and "delay–Doppler imaging," where we sort the echo power into received time (delay) and frequency. Our reduction of raw echo power spectra included background removal, calibration, and the formation of sums of spectra weighted by signal strength. We measured the radar cross-sections of our targets, in km^2, σ_{OC} and σ_{SC}, by integrating the CW power spectra. These are equivalent to the cross-sectional areas of a smooth, metallic sphere (a perfect reflector) that would generate the observed echo power when viewed at the same distance.

For an asteroid observed at S-band (2380-MHz), its plane-of-sky extent (in km) normal to the apparent spin vector at rotation phase ϕ, $D(\phi)$, is related to the instantaneous bandwidth B of the radar echo (due to the apparent rotation), the target's physical properties, and its orientation by

$$D(\phi) = \frac{P B(\phi)}{27.7 \cos\delta}, \tag{2}$$

where P is the apparent (synodic) rotation period in hours and δ is the subradar latitude. For each target we estimate the minimum bandwidth and the corresponding lower bound on the maximum pole-on breadth, D_{max}, using Eq. (2). Our experience with asteroids of modest signal-to-noise ratio (optimally filtered sum SNR $> \sim$20) suggests that a reasonable estimate of the bandwidth can be made from the points where the echo power spectrum first drops to two standard deviations of the background noise, written as $B_{2\sigma}$. Uncertainties for this estimate are based on the crossing points at 1- and 3-standard deviations of noise.

Bandwidths for our weaker targets are estimated using the points where echo power drops to zero standard deviations (zero-crossing or B_{ZC}) after folding the spectrum about 0 Hz and smoothing in frequency to boost SNR (Magri et al., 1999). Uncertainties are typically based on the frequency resolution of the spectrum. In cases where we have rotationally resolved data and wish to measure variations in the bandwidth, we use the equivalent bandwidth (B_{EQ}) because it is less sensitive to noise than other methods and is a conservative lower limit on the bandwidth. It can be calculated from

$$B_{EQ} = \frac{(\sum_i S_i)^2}{\sum_i (S_i)^2} \Delta f, \tag{3}$$

where Δf is the frequency channel width and S_i is the signal in the ith channel (Tiuri, 1964; see Magri et al., 1999, for more discussion of its properties). Like all bandwidth estimators, B_{EQ} changes as we smooth the signal in frequency. However, as the signal is filtered with increasingly larger bandwidth filters, B_{EQ} quickly reaches a stable value. To estimate B_{EQ}, we smooth our spectra until the value plateaus. We estimate the uncertainty in this parameter as twice the width of the filter at which B_{EQ} stabilizes.

The circular polarization ratio, μ_c, is defined to be the ratio of the SC and OC echo power:

$$\mu_c = \frac{\sigma_{SC}}{\sigma_{OC}}. \tag{4}$$

Values larger than zero are thought to be caused by wavelength-scale near-surface roughness and inhomogeneities and/or subsurface or multiple scattering. Smooth surfaces have polarization ratios approaching 0.0, while some extremely rough surfaces have values near or at unity (Ostro et al., 1985).

The OC radar albedo, $\hat{\sigma}_{OC}$, of an asteroid is defined to be the ratio of its OC radar cross-section (σ_{OC}) to its cross-sectional area,

$$\hat{\sigma}_{OC} = \frac{4\sigma_{OC}}{\pi D_{eff}^2}. \tag{5}$$

$\hat{\sigma}_{OC}$ can vary with rotation and aspect. Published asteroid radar albedos vary from a low of 0.039 for the CP-class main-belt Asteroid (MBA) 247 Eukrate (Magri et al., 2007a, 2007b) to a maximum of 0.6 for the M-class 216 Kleopatra (Ostro et al., 2000). For a summary of asteroid radar properties, see http://echo.jpl.nasa.gov/~lance/asteroid_radar_properties.html.

Uncertainties in our estimates of absolute radar cross-section are usually ±25% and are based on estimates of systematic uncertainties in transmitted power and calibration. Targets with low SNR ($\sim$10 or less) have quoted uncertainties up to 50%. Relative uncertainties in radar cross-section are on the order of 10% for observations made on the same target over a few days. Because systematic uncertainties are nearly the same for both polarization senses, our uncertainties in circular polarization ratio are dominated by receiver thermal noise. Unless otherwise stated, our quoted uncertainties for random errors are one-standard deviation.

2.3. Estimating bulk density and metal content from radar cross-section

The radar albedo of an asteroid is a function of the physical properties of the near-surface, i.e., from the space–regolith interface to a depth of several wavelengths. To first order, the echo power is controlled by the bulk density of the near-surface and by the amount of wavelength-scale roughness. Estimating the bulk density of an asteroid surface has been the subject of several models, most recently by Ostro et al. (1985, 2000) and Magri et al. (2001). In this paper, we wish to use a simple decision tool: based on an asteroid's OC radar albedo and circular polarization ratio, is it (a) likely to be dominantly metallic, or (b) unlikely to be dominantly metallic? To develop this further, we make the following assumptions. (1) The large main-belt asteroids accessible to radar have a developed surface regolith that is at least a few tens of centimeters in depth so that this is the interface involved in the echo. There is no significant region that is regolith-free. (2) The asteroid near-surface has a porosity of 50 ± 10%, similar to core samples from the uppermost meter of the Moon (Carrier et al., 1991). (3) Given their spectral properties, the most likely meteorite analogs for M-class asteroids and their associated grain densities are irons (7.5 g cm^{-3}), CH/CB/bencubbinite (metal rich) carbonaceous chondrites or silicate-bearing iron meteorites (5.0 g cm^{-3}), enstatite chondrites (3.5 g cm^{-3}), and carbonaceous chondrites (2.5 g cm^{-3}) (Bell et al., 1989; Gaffey, 1976; Vilas, 1994; Hardersen et al., 2002).

We used both the uncalibrated and the Eros-calibrated ('calibrated' hereafter) models of Magri et al. (2001) to estimate the

Table 2
Model OC radar albedos for various meteorite analogs

Model	Carbonaceous chondrites	Enstatite chondrites	CH/CB/bencub. Si-bearing irons	NiFe irons
Eros calibrated	0.11 ± 0.01	0.22 ± 0.01	0.43 ± 0.01	0.85 ± 0.05
Eros uncalibrated[a]	0.08 ± 0.04	0.16 ± 0.05	0.28 ± 0.07	0.47 ± 0.12

[a] Assumes porosity 0.5 ± 0.1 and $\mu_c = 0.2$.

range of OC radar albedos expected for potential M-class constituents and our assumed near-surface porosities. Adoption of the Eros-calibrated model includes the implicit assumption that our asteroids have near-surface properties similar to Eros, differing only in Fresnel reflectivity. Eros was observed to have a significant regolith, consistent with our first assumption, and its circular polarization ratio is $\mu_c = 0.28 \pm 0.06$, similar to several previously observed M-class MBAs (Table 1; Magri et al., 2007a) but considerably higher than 216 Kleopatra and 22 Kalliope. Our expected OC radar albedos for the different constituents are listed in Table 2. The uncertainties reflect the range in potential porosities. The calibrated model makes systematically higher predictions for radar albedo than the uncalibrated model and is generally insensitive to variations in assumed porosity, especially for lower density materials.

3. Results

3.1. 16 Psyche

Psyche is the largest M-asteroid known, with an IRAS diameter of 253 ± 4 km and an IRAS-derived visual albedo of $p_v = 0.10$ (Tedesco et al., 2002). Based largely on lightcurve analyses, a number of authors have reported poles for Psyche, most of which are compiled in the Small Bodies Node of the Planetary Data System (PDS) (Magnusson, P., Neese, C. (Eds.), 1996. Asteroid Spin Vectors. EAR-A-5-DDR-ASTEROID-SPIN-VECTORS-V4.2. NASA Planetary Data System). Kaasalainen et al. (2002) used lightcurves from 19 apparitions and derived a convex shape model for Psyche with axes ratios $a/b \sim 1.2$ and $b/c \sim 1.2$, a rotation period $P = 4.195947 \pm 0.000001h$, and two possible poles at ecliptic coordinates $(\lambda, \beta) = (216°, -2°)$ and $(35°, -9°) \pm 5°$. They also report an apparent 'bright spot' on one side of Psyche; a similar report was made by Dotto et al. (1992).

Given that information about Psyche's IRAS diameter, mass estimates of Psyche lead to unexpectedly low bulk densities of 1.4–1.8 g cm^{-3} (Viateau, 2000; Kochetova, 2003) suggesting a bulk porosity of order of 70% for metallic compositions (Britt et al., 2002). In part because of this unusual result, a number of workers have employed other techniques to estimate Psyche's size.

Cellino et al. (2003) report speckle interferometry observations of Psyche and report 'a' and 'b' apparent diameters of 315 ± 60 and 262 ± 46 km, respectively, giving an average apparent size of 288 ± 43 km. This is larger than but consistent with the IRAS diameter to within the quoted uncertainties.

Lupishko (2006) revised the diameter estimate of Psyche to 213 km by using a visual albedo of 0.17 based on polarimetric measurements. This diameter leads to a bulk density estimate $\rho_{\text{bulk}} = 3.3 \pm 0.7$ g cm^{-3}, giving a porosity estimate of 30–40% for metallic compositions.

In more recent work, Drummond and Christou (2006) used adaptive optics at the Lick 3.0 m telescope to image Psyche directly on two occasions. They report a best fit to a triaxial ellipsoid of dimensions 283 ± 16 km $\times 216 \pm 25$ km $\times 151 \pm 9$ km ($a/b = 1.3$, $b/c = 1.4$), giving $D_{\text{eff}} = 210 \pm 16$ km, consistent with the Lupishko (2006) size and porosity estimates. They report a pole direction of $(\lambda, \beta) = (36°, -3°) \pm 7°$, consistent with one of the Kaasalainen et al. (2002) poles.

Magri et al. (1999) report radar observations of Psyche in 1980 and 1985 with total experiment SNRs of 10 and 16, respectively. For the two dates, they report OC radar cross-sections $\sigma_{\text{OC}} = 14{,}000$ and 14,300 km^2 (±25%), and polarization ratios of $\mu_c = 0.14 \pm 0.10$ and 0.18 ± 0.06, respectively. Assuming the IRAS diameter, they calculated a radar albedo $\hat{\sigma}_{\text{OC}} = 0.31 \pm 0.08$.

We observed Psyche on five nights, 12–16 November 2005 (Table 3), obtaining a total of eight CW runs and three delay–Doppler images. Our integration times were long enough and of sufficient SNR to split each CW run into two, giving us 16 observations (Fig. 1, Table 4). Our weighted sum of all CW runs has SNR of 67, bandwidth $B_{2\sigma} = 855 \pm 50$ Hz, an OC radar cross-section $\sigma_{\text{OC}} = 15800 \pm 4000$ km^2, and a polarization ratio $\mu_c = 0.06$ (Fig. 2). The OC radar cross-section is consistent, to within the uncertainties, those values reported by Magri et al. (1999) (Table 5), but the polarization ratio is considerably lower. Looking at Table 4, we find that our polarization ratios are bimodal with values tending to cluster in ranges 0.00–0.07 and 0.13–0.18; this latter range is consistent with previously reported polarization ratios. The sum of our three images has a bandwidth $B_{2\sigma} = 780 \pm 100$ Hz, consistent with the CW result, and a delay-depth of 42 ± 10 km, suggesting a diameter of about 84 ± 20 km, considerably smaller than the expected radius of Psyche (Fig. 3). This latter observation is most likely because the low SNR of these runs (∼20 for the sum) prevents us from seeing the full range depth; however, it is also possible that (1) Psyche is somewhat limb darkened in the radar, (2) smaller than reported, or (3) some combination of the two.

If Psyche were a perfectly reflecting (metallic) sphere, then our nominal OC cross-section suggests a lower bound on $D_{\text{eff}} \sim 150$ km. Our bandwidth estimate, $B_{2\sigma} = 855$ Hz, known rotation period, and expected subradar latitude from the Kaasalainen et al. (2002) poles ($\delta = 45°$) leads to a maximum diameter estimate $D_{\max} = 183 \pm 20$ km. This value is significantly lower than expected from previous estimates and we believe Psyche's low circular polarization ratio and lower-than-expected delay-depth may indicate limb darkening and result in an underestimate of the spectral edges. We therefore adopt the largest bandwidth consistent with our data to estimate spectral edges, $B_{\text{ZC}} = 1066 \pm 50$ Hz. In Fig. 4 we plot contours of $D_{\max}$ consistent with this bandwidth along with all previously published poles (Magnusson, P., Neese, C. (Eds.), 1996. Asteroid Spin Vectors. EAR-A-5-DDR-ASTEROID-SPIN-VECTORS-V4.2. NASA Planetary Data System; and those above). Only

Table 3
Observing circumstances

Target	Date	RA (°)	DEC (°)	λ (°)	β (°)	Dist. (AU)	Runs	OC SNR	Mode	Start–stop
16 Psyche	2005 Nov 12–16	80	18	81	−5	1.73	8	67	CW	04:15–06:29
	2005 Nov 15,17	80	18	80	−5	1.73	3	–	70 μs	05:14–07:03
21 Lutetia	2004 Oct 18, 20–21	42	12	44	−4	1.25	7	–	40 μs	04:01–06:49
71 Niobe	2006 Feb 20–22	148	3	149	−10	1.55	4.5	20	CW	03:37–05:01
97 Klotho	2006 Dec 22	90	2	90	−21	1.06	1	65	CW	04:50–05:07
129 Antigone	2005 Apr 28–May 1	231	4	228	21	1.32	7	51	CW	04:51–06:20
	2005 May 12–13	229	4	225	22	1.31	2	26	CW	03:45–04:25
135 Hertha	2004 Sep 20	16	9	18	2	1.06	1	33	CW	06:05–06:22
	2004 Oct 11	11	7	13	2	1.07	3	37	CW	03:10–04:39
224 Oceana	2004 Oct 12–13, 18	12	9	15	4	1.67	4	12	CW	03:15–04:38
325 Heidelberga	2004 Nov 16–17	34	26	40	12	1.70	4	14	CW	02:36–03:46
758 Mancunia	2006 Dec 22–24	72	18	73	−4	1.77	5	39	CW	01:47–04:17
785 Zwetana	2005 Apr 28–May 1	211	4	206	16	1.06	9	40	CW	03:19–04:58
	2005 May 12–13	208	3	205	14	1.10	4	19	CW	02:25–03:36

RA, DEC are J2000 at center of observation window. λ and β are the ecliptic longitude and latitude.
Dist. is the Earth–asteroid distance.
Runs is the number of transmit-receive cycles. A half run indicates we only received ∼50% of total integration time.
Setup mode is continuous wave (CW) or delay–Doppler imaging with the baud rate shown. The Psyche data were sampled twice per baud, giving an effective resolution of 35 μs per delay bin. Multiple samples per baud result in correlated range pixels.
Start–stop gives the beginning and end of a series of runs, from first to last reception (in UTC).

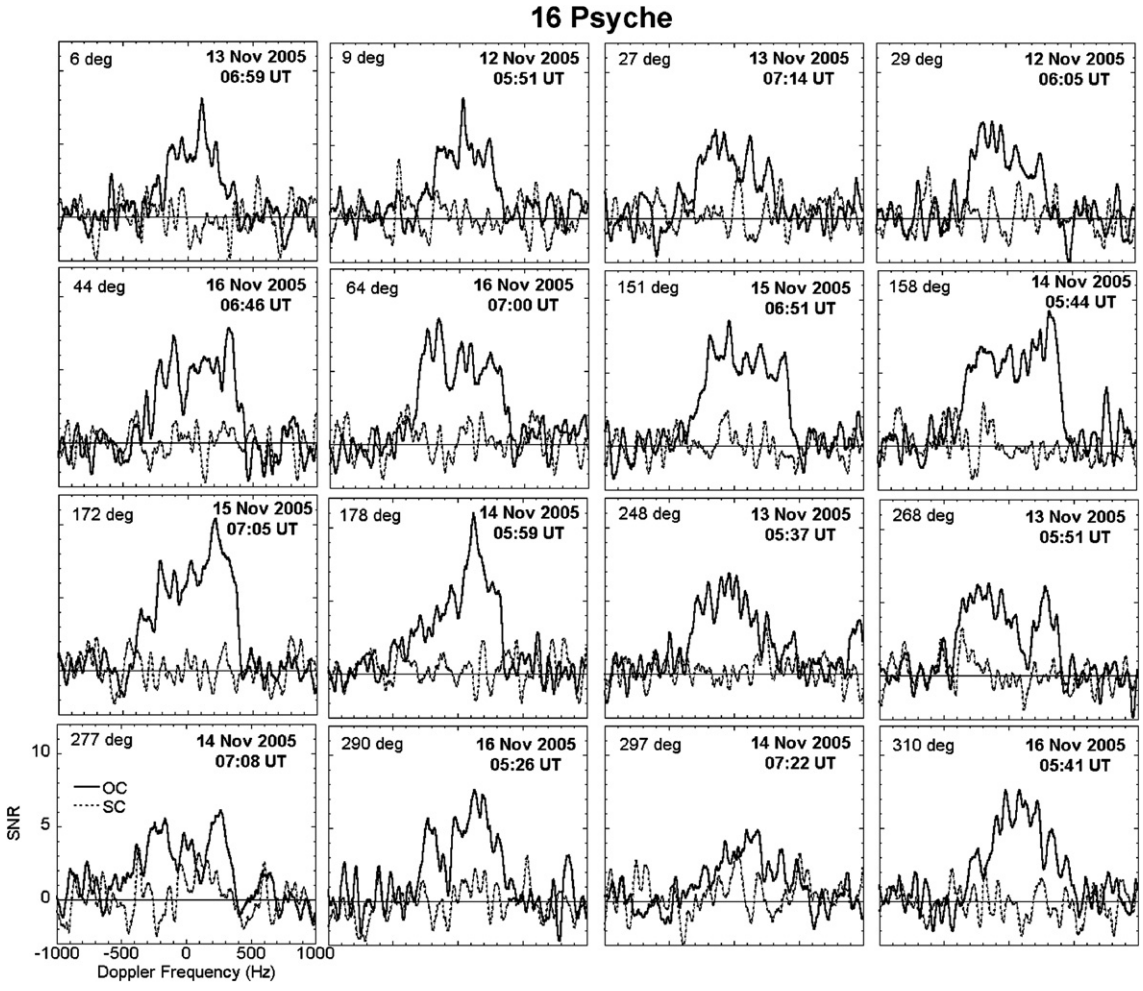

Fig. 1. Mosaic of CW spectra of Psyche, smoothed to 50 Hz effective frequency. Dates, times, and relative rotation phases are shown. Epoch for 0° rotation phase is 12 Nov 2005 05:45 UTC.

Table 4
CW radar properties of individual targets

Asteroid	Date	Time UT	SNR	ϕ/lon (°)	B (Hz)	σ_{OC} (km^2)	μ_c
16 Psyche	2005 Nov 12	5:51	15	9	637 ± 100	12,200	0.18 ± 0.03
	2005 Nov 12	6:05	15	29	613 ± 100	13,200	0.18 ± 0.03
	2005 Nov 13	5:37	17	248	761 ± 100	15,900	0.04 ± 0.02
	2005 Nov 13	5:51	16	268	718 ± 100	15,400	0.02 ± 0.02
	2005 Nov 13	7:00	14	6	455 ± 100	10,900	0.00 ± 0.02
	2005 Nov 13	7:14	13	27	562 ± 100	12,200	0.13 ± 0.03
	2005 Nov 14	5:45	22	158	764 ± 100	21,600	0.00 ± 0.02
	2005 Nov 14	5:59	20	178	777 ± 100	21,000	0.18 ± 0.03
	2005 Nov 14	7:08	14	277	826 ± 100	16,000	0.16 ± 0.03
	2005 Nov 14	7:22	11	297	513 ± 100	9,500	0.38 ± 0.03
	2005 Nov 15	6:51	21	151	769 ± 100	21,300	0.00 ± 0.02
	2005 Nov 15	7:05	24	172	729 ± 100	22,500	0.00 ± 0.02
	2005 Nov 16	5:27	17	290	613 ± 100	14,000	0.00 ± 0.02
	2005 Nov 16	5:41	18	310	614 ± 100	14,200	0.03 ± 0.02
	2005 Nov 16	6:46	18	44	531 ± 100	14,400	0.05 ± 0.03
	2005 Nov 16	7:00	20	64	712 ± 100	18,000	0.07 ± 0.02
	Sum of dates	–	67	–	1066 ± 50	15,800	0.06 ± 0.02
71 Niobe	2006 Feb 20		15	0	73 ± 20	1260	0.16 ± 0.03
	2006 Feb 21		13	241	58 ± 20	1010	0.15 ± 0.03
	2006 Feb 22		12	122	50 ± 20	870	0.57 ± 0.07
	Sum of dates	–	20	–	75 ± 15	1020	0.22 ± 0.05
97 Klotho	2006 Dec 22	–	65	–	75 ± 10	1420	0.24 ± 0.02
129 Antigone	2005 Apr 28	5:26	30	232	291 ± 4	4780	0.08 ± 0.03
	2005 Apr 28	6:10	12	179	222 ± 40	3890	0.30 ± 0.08
	2005 Apr 29	4:52	24	330	358 ± 40	4660	0.10 ± 0.05
	2005 Apr 29	5:36	30	277	395 ± 40	5230	0.15 ± 0.04
	2005 Apr 30	5:12	13	2	292 ± 40	2180	0.14 ± 0.07
	2005 May 1	4:57	17	78	243 ± 40	2620	0.05 ± 0.05
	2005 May 1	5:41	11	25	166 ± 40	1820	$0.00 + 0.08$
	2005 May 12	4:14	13	34	263 ± 40	2130	0.35 ± 0.08
	2005 May 13	3:56	24	137	387 ± 40	4360	0.08 ± 0.04
	Sum of dates	–	58	–	440 ± 20	3580	0.14 ± 0.02
135 Hertha	2004 Sep 20	06:13	33	0	193 ± 50	1110	0.02 ± 0.03
	2004 Oct 11	03:19	25	233	199 ± 50	850	0.17 ± 0.04
	2004 Oct 11	03:54	24	258	143 ± 50	685	0.08 ± 0.04
	2004 Oct 11	04:30	17	283	200 ± 50	620	0.11 ± 0.06
	Oct 11 sum	–	37	258	206 ± 50	720	0.13 ± 0.03
	Sum of dates		48		225 ± 25	810	0.10 ± 0.03
224 Oceana	2004 Oct 12–13, 18	–	12	–	175 ± 15	750 ± 300	0.33 ± 0.06
325 Heidelberga	2004 Nov 16–17	–	14	–	270 ± 30	775 ± 400	0.0 ± 0.1
758 Mancunia	2006 Dec 22	2:46	16	134	160 ± 30	2480	0.33 ± 0.05
	2006 Dec 22	4:03	14	170	180 ± 30	2720	0.41 ± 0.06
	2006 Dec 23	2:37	25	88	150 ± 30	3840	0.24 ± 0.04
	2006 Dec 24	2:31	14	43	190 ± 30	2980	0.38 ± 0.05
	2006 Dec 24	3:53	20	82	150 ± 30	3860	0.21 ± 0.05
	Sum of dates	–	39	–	207 ± 20	3250	0.34 ± 0.03
785 Zwetana	2005 Apr 28	4:15	24	100	106 ± 20	965	0.13 ± 0.04
	2005 Apr 28	4:50	9	124	117 ± 20	520	0.40 ± 0.11
	2005 Apr 29	3:39	5	328	43 ± 20	170	1.00 ± 0.40
	2005 Apr 29	4:13	7	351	136 ± 20	360	0.08 ± 0.08
	2005 Apr 30	3:28	19	212	107 ± 20	895	0.09 ± 0.06
	2005 Apr 30	4:02	26	236	122 ± 20	1140	0.04 ± 0.04
	2005 Apr 30	4:37	13	259	111 ± 20	685	0.17 ± 0.08
	2005 May 1	3:46	15	117	92 ± 20	605	0.18 ± 0.07
	2005 May 1	4:22	6	141	107 ± 20	260	0.74 ± 0.20
	2005 May 12	2:51	5	332	83 ± 20	260	0.37 ± 0.20
	2005 May 12	3:28	7	355	93 ± 20	410	0.16 ± 0.12

(*continued on next page*)

Table 4 (*continued*)

Asteroid	Date	Time UT	SNR	ϕ/lon (°)	B (Hz)	σ_{OC} (km^2)	μ_c
	2005 May 13	2:34	13	213	112 ± 20	770	0.13 ± 0.08
	2005 May 13	3:10	16	237	118 ± 20	860	$0.00 + 0.07$
	Sum of dates	–	44	–	160 ± 10	615	0.17 ± 0.03

Time and date are the mid-times of acquisition (UT). ϕ is rotation phase starting from an arbitrary epoch (degrees) except for Antigone, where it is the shape-model based longitude (lon). In that system, lon 0° is along $+x$-axis, 90° is along $+y$-axis and rotation phase can be found from $\phi = 360 - \text{lon}$. B is bandwidth (Hz). For individual runs, we list B_{EQ}, which is less sensitive to noise, to give a sense of the variation in bandwidth. The bandwidth listed for the total experiment is B_{ZC} (Psyche, Oceana, and Heidelberga) or $B_{2\sigma}$ (all others). σ_{OC} is the OC radar cross-section (km^2), and μ_c is the polarization ratio. Uncertainties in radar cross-section are 25% unless noted otherwise.

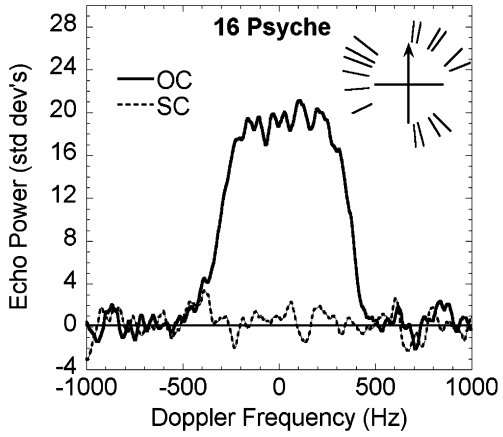

Fig. 2. Sum of all Psyche CW spectra smoothed to 50 Hz. Relative rotation phase at mid-epoch for each run is shown in the upper right figure. The arrow indicates 0° phase selected to be 12 Nov 2005 05:45 UTC.

Table 5
Previous Psyche radar observations

Date	SNR	λ, β (°)	σ_{OC} (km^2)	μ_c	B_{ZC} (Hz)
1980	10	78, −5	$14{,}000 \pm 3700$	0.14 ± 0.10	840 ± 40
1985	16	73, −5	$14{,}300 \pm 3700$	0.18 ± 0.06	875 ± 100
2005	67	81, −4	$15{,}800 \pm 4000$	0.06 ± 0.02	1066 ± 50

Data from Magri et al. (1999) and this work.

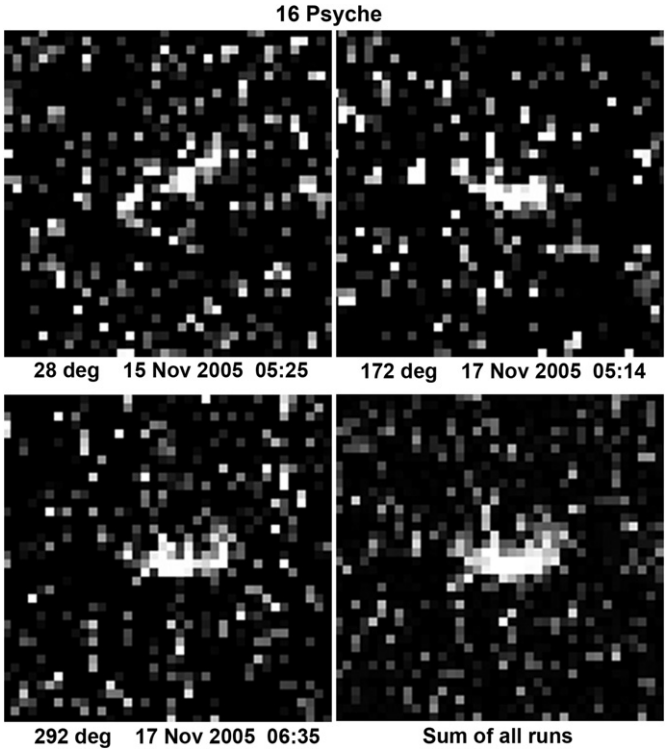

Fig. 3. Mosaic of our three delay–Doppler images of 16 Psyche and their sum. Times (UTC) and relative rotation phases are indicated. Each pixel is 56 Hz (horizontal axis) by 35 μs (5.25 km along vertical axis). Delay increases from bottom to top, frequency from left to right. Each image is 2100 Hz (460 km) × 1318 μs (198 km).

a handful of published poles are consistent with our data and $D_{max} \geqslant 225$ km and none are consistent with $D_{max} > 270$ km, even including our uncertainties in B_{ZC}. All of the poles consistent with our data are clustered, so we average them into a 'synthesis' pole $(\lambda, \beta) = (37°, -5°) \pm 5°$ or $(218°, +3) \pm 5°$ (shown as crosses) and, including the uncertainties in our estimate of B_{ZC}, adopt $D_{max} = 240 \pm 35$ km. These poles are consistent with those reported by Kaasalainen et al. (2002).

A plot of CW bandwidth versus rotation phase (Fig. 5) shows only one maximum at ∼180° and one minimum at 0° per cycle and is consistent with the single maximum/minimum observed in many lightcurves. This is also consistent with previous suggestions that a triaxial ellipsoid may not be the best model for this asteroid (Zappala and Knezevic, 1984), although that conclusion may be erroneous if there are albedo variations on Psyche's surface as reported by others (Kaasalainen et al., 2002; Dotto et al., 1992; Weidenschilling et al., 1990). The total variation in bandwidth is ∼1.4, similar to the a/b value reported by Drummond and Christou (2006) but slightly higher than the Kaasalainen et al. (2002) value of 1.2. In short, Psyche does not appear to be elongate but may have a complex shape or radar and visual albedo variations. We reserve shape modeling for future work.

Both Kaasalainen et al. (2002) and Drummond and Christou (2006) give estimates of Psyche's axis ratios. We average their two a/b estimates with our bandwidth variations and obtain axis ratios $a/b = 1.3 \pm 0.1$ and (averaging just their estimates) $b/c = 1.3 \pm 0.1$. Assuming these values, we obtain an ellipsoid model with axes $240 \times 185 \times 145$ km $\pm$ 15%. We adopt this as our nominal model and obtain $D_{eff} = 186 \pm 30$ km, smaller than but consistent with, to within uncertainties, the size estimates of Lupishko (2006) and Drummond and Christou (2006), and considerably smaller than the IRAS or Cellino et al. (2003) size estimates. This model leads to a visual albedo estimate of $p_v = 0.23 \pm 0.05$ and an initial radar albedo estimate of $\hat{\sigma}_{OC} = 0.58 \pm 0.15$, both of which are consistent with

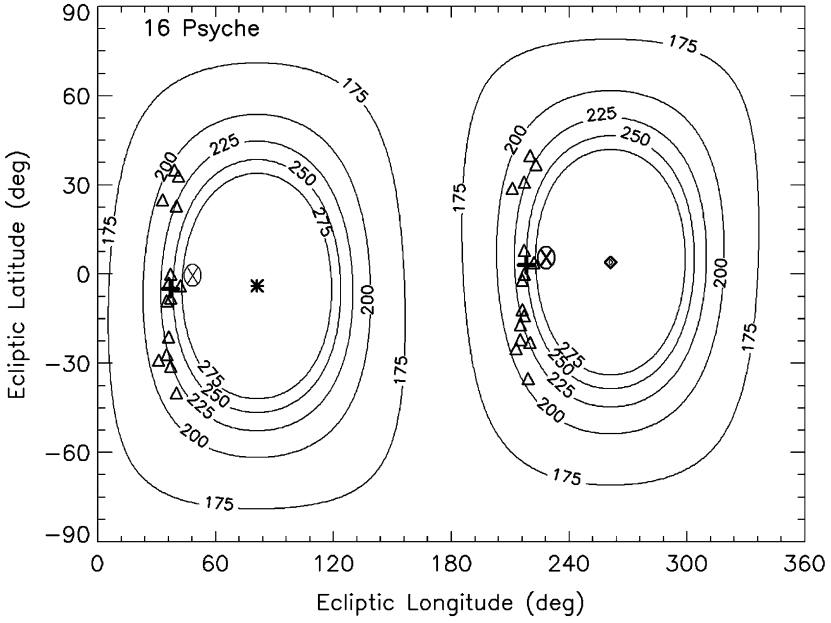

Fig. 4. Contours of Psyche's $D_{\max}$ (in km) for a bandwidth of 1066 Hz (Eq. (2)). Psyche's position during this encounter is shown with an asterisk; the mirror position is a small diamond. Previously published poles are shown as triangles. The crosses indicate our adopted synthesis poles. The circled 'X' indicates the position of Psyche during the IRAS measurements (bold X, on the right) and its mirror (not-bold, on the left).

the expected range for a metallic M-class asteroid. [*Note added in proof*. Given the most recent mass estimate of Psyche (Baer and Chesley, 2008), our adopted size leads to a bulk density estimate of $7.6 \pm 3\ \mathrm{g\,cm^{-3}}$, implying a significant metal fraction.]

Why are our and more recent estimates of Psyche's diameter considerably smaller than the IRAS estimate? We note that at the time of the IRAS observations Psyche was at ecliptic position $\lambda = 225°$, $\beta = 3°$ (circled X in Fig. 4), presenting a nearly pole-on view to both the Earth and Sun and leading to a probable overestimate of its effective diameter. If IRAS only viewed our model '*a*' and '*b*' axes, it would be effectively observing an object 215 km in diameter which is within 15% of the IRAS value. However, we find that our axes estimates are not consistent with those reported by Cellino et al.

Plots of radar cross-section versus rotation phase mimic the bandwidth plot but show a much larger variation (Fig. 5); where we observe up to 40% variation in the bandwidth with rotation, we observe more than 100% variation in radar cross-section. Because we observed comparable values on different days, we conclude that the variations are real. We normalized the ratio of radar cross-section to projected area (giving radar albedo) as follows. We made the assumption that the projected area is proportional to the Doppler bandwidth (B_{EQ}). We fit a second-order polynomial to our plot of B_{EQ} vs rotation phase and used this polynomial as a proxy for projected area. The area at 0° rotation phase ($B_{\mathrm{EQ}} \sim 510$ Hz and near the minimum of estimated bandwidth) was set equal to the smallest projected area of our ellipsoid (2.9×10^4 km^2, $D_{\mathrm{eff}} = 192$ km), assuming a subradar latitude of 45° (based on our synthesis pole). The maximum projected area for this bandwidth-based model is 4.5×10^4 km^2 ($D_{\mathrm{eff}} = 239$ km). When normalized by this method, the radar albedo has a mean value $\hat{\sigma}_{\mathrm{OC}} = 0.42$ and ranges from 0.26 to 0.51. (Note that our simple ellipsoid model would have a maximum projected area of 3.1×10^4 km^2 at this subradar latitude, significantly less than we estimate from this B_{EQ} proxy; if anything, our method overestimates the projected area and underestimates the radar albedo.) This large radar albedo range suggests the existence of a radar anomaly on one side of Psyche. As noted earlier, Kaasalainen et al. (2002) report the existence of a large albedo 'spot' on one side of Psyche which may be related. Binzel et al. (1995) obtained rotationally resolved spectra of Psyche at a near equatorial aspect and report no spectral variation larger than 1%. This argues against compositional heterogeneity and suggests that an unusual surface feature or texture is more likely responsible for both anomalies. We also note that

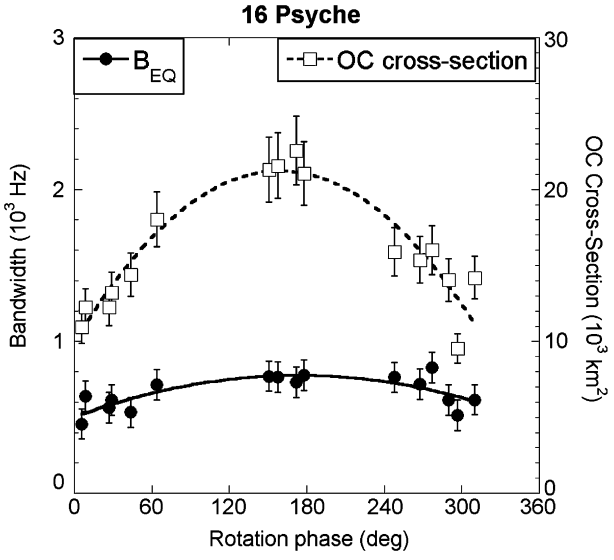

Fig. 5. Bandwidth and OC cross-section of Psyche as a function of its rotation phase. Bandwidth is the band-width equivalent (B_{EQ}) of a 50 Hz smoothed spectrum with uncertainties of ±100 Hz. Relative uncertainties on cross-section are 10%. Lines are best fit second order polynomials to the data used to model radar albedo (see text).

there appears to be an inverse correlation of OC radar albedo and polarization ratio, suggesting that some of the variation in radar albedo may be due to variations in surface roughness and not composition. Future shape modeling work may help determine if our radar anomaly is consistent with the albedo 'spot' and resolve these other issues.

3.2. 21 Lutetia

Lutetia has been the subject of increased study recently because it is a target for the Rosetta spacecraft with a flyby scheduled in July 2010 (Fulchignoni et al., 2004). Based on IRAS observations (Tedesco et al., 2002), Lutetia's effective diameter is $D_{\rm eff} = 96 \pm 4$ km and its visual albedo is $p_v = 0.22 \pm 0.02$. More recent thermal measurements and modeling by Mueller et al. (2005) are consistent with this and give $D_{\rm eff} = 98 \pm 6$ km.

Magri et al. (1999) reported radar observations of Lutetia made in October 1985 at Arecibo and modeled Lutetia as an ellipsoid of dimensions $130 \times 104 \times 74$ km ($\pm 17\%$), with axis ratios of $a/b = 1.25 \pm 0.15$ and $b/c = 1.4 \pm 0.3$. They reported two possible poles: $(\lambda, \beta) = (228^\circ \pm 11^\circ, +13^\circ \pm 5^\circ)$ and $(48^\circ \pm 11^\circ, +5^\circ \pm 5^\circ)$.

Torppa et al. (2003) presented a convex shape model of Lutetia based on 36 lightcurves from six apparitions. They obtained a shape characterized by sharp and irregular features and no evidence of albedo variegations. They reported two possible poles: $(\lambda, \beta) = (39^\circ, 3^\circ)$ or $(\lambda, \beta) = (220^\circ, 3^\circ)$. Both poles have uncertainties of $\pm 10^\circ$ and are, within the uncertainties, consistent with the poles of Magri et al. Their model has axis ratios $a/b = b/c = 1.2$. Using the newer Torppa et al. pole directions, Magri et al. (2007a) revised their previous ellipsoid estimate to $120 \times 100 \times 83$ km ($D_{\rm eff} = 100 \pm 11$ km).

Rivkin et al. (2000) reported the detection of a 3 μm water-of-hydration feature in the spectra of Lutetia, interpreted to be caused by hydrated minerals. Recent spectral evidence has led to the conclusion that Lutetia's class is more likely C than M, with CI meteorites, and specifically Orgueil, the best spectral match to ground-based spectra (Nedelcu et al., 2006). CI meteorites contain hydrated minerals, consistent with the 3 μm feature observed by Rivkin et al. However, Orgueil is dark, with laboratory reflectances of ∼5% (Johnson and Fanale, 1973). Thus a conundrum: are the estimated albedo and size incorrect? Or are there bright analogs to the CI meteorites in the asteroid population?

We observed Lutetia on four nights at Arecibo in October 2004. The first night's observations were at a much coarser resolution than the other three and are not included in this analysis. All observations were delay–Doppler imaging, and we show daily sums from the three nights and their sum in Fig. 6. We attempted to use our observations and previous lightcurves to generate a 3D shape model. Unfortunately, our observations were within a few degrees of the pole and our model solutions were sensitive to even 1° variations in the subradar latitude; additionally, solutions this close to the pole are subject to significant ambiguities. As a result, we were unable to generate a unique shape model.

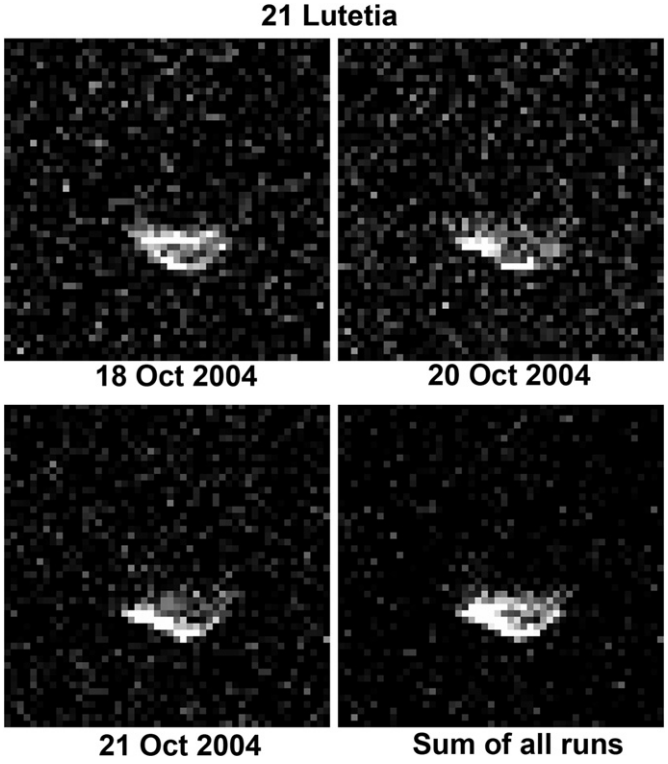

Fig. 6. Daily sums of delay–Doppler images (18–21 Oct) of Lutetia and the sum of all observations (lower right). Each image has a resolution of 4 Hz (horizontal axis) by 40 μs (6 km, vertical axis) and a total extent of 200 Hz by 2000 μs (300 km). Delay increases from bottom to top; Doppler frequency increases from left to right.

Despite this difficulty, our observations add constraints to what is known about Lutetia. The bandwidth of the image sum is $B_{2\sigma} = 68 \pm 4$ Hz and the delay-depth is 280 ± 40 μs, or 42 ± 6 km. Since our delay-depth is viewing essentially along the asteroid c-axis, this suggests a c-axis of ∼2× our delay-depth, or 84 ± 12 km, consistent with the revised ellipsoid model of Magri et al. (2007a). Our bandwidth results in a nominal estimate of $D_{\rm max} = 20.1\ {\rm km}/\cos\delta$. Assuming the Magri et al. (2007a) value for $D_{\rm max}$ (120 km), the subradar latitude at the time of our observations was 87°. This is exactly as predicted by the Torppa et al. $(\lambda, \beta) = (220^\circ, 3^\circ)$ pole, and within the uncertainties of the $(\lambda, \beta) = (39^\circ, 3^\circ)$ pole.

After calibrating the images using methods described by Magri et al. (2007a) and assuming their revised ellipsoid model, we estimate an OC radar cross-section of $\sigma_{\rm OC} = 2250$ km^2 ($\pm 25\%$) and an OC radar albedo of $\hat{\sigma}_{\rm OC} = 0.24 \pm 0.07$; these values are larger than, but within the uncertainties, of those reported by Magri et al. (1999) (Table 1).

Based on these and previous data, there seems little doubt that Lutetia's effective diameter and visual albedo are $D_{\rm eff} = 100 \pm 11$ km and $p_v = 0.20 \pm 0.03$. The radar albedo is not consistent with a largely metallic object like Kleopatra or Psyche, but is considerably higher than the mean C-class asteroid value of 0.13 ± 0.05, suggesting a higher near-surface bulk density than the typical C-class asteroid. Additionally, Lutetia's visual albedo is anomalously high for a C-class asteroid, especially one linked closely with CI meteorites. A possible solution to this problem was suggested by Rivkin et al. (2000).

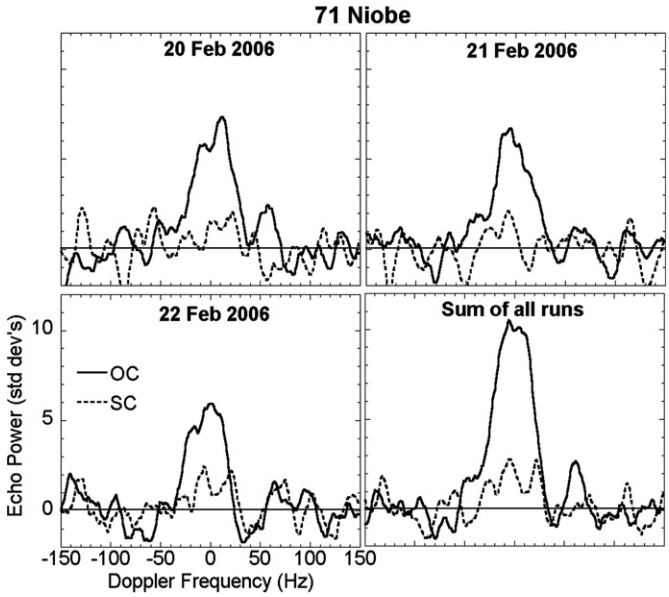

Fig. 7. Daily sums and sum of all CW runs for Niobe, smoothed to 15 Hz effective frequency resolution.

He notes work by Zolensky and McSween (1988) and Fanale et al. (1974) on high albedo hydrated salts that occur in veins in CI meteorites, and in particular in Orgueil. Lutetia's albedo would be explained if these salts were previously mobilized by water and are now present in moderate abundance (∼30%) on the surface. Given that Torppa et al. (2003) find no evidence of albedo variegation, the high albedo material would have to be distributed globally.

3.3. 71 Niobe

Niobe is an S-class object in the Tholen (1984) taxonomy and S0 in the Barucci et al. (1987) taxonomy. However, Bus and Binzel (2002) classify it as an Xe-class, the same classification given to 216 Kleopatra, so we included it in our survey. Niobe's IRAS diameter is $D_{\rm eff} = 83 \pm 2$ km and its visual albedo is at the high end of expected M-class asteroids, $p_v = 0.31 \pm 0.01$. No pole has been reported for Niobe.

Niobe's period had been reported to be $P = 14.4$ h (Harris and Young, 1989), but this was based on incomplete coverage. Warner et al. (2006) obtained lightcurve data over ten nights in February 2006. Those data yield a period of $P = 35.6 \pm 0.1$ h, and have an amplitude of 0.22 mag, suggesting a modestly elongate object. Long-term follow-up work by Sada and Warner (2007) refined the period to $P = 35.81 \pm 0.01$ h. The previously reported period appears to be a 2:5 alias of the true period.

We observed Niobe on three nights, 20–22 February 2006, and acquired 1.5 runs per night (a "half" run results when we only obtain ∼half of the possible integration time because the object exits the telescope observing window). The SNR of an optimally filtered sum of all runs is 20. Fig. 7 shows our daily sums of spectra and our weighted sum of all runs, while the radar properties of our runs are listed in Table 4. To within uncertainties, our bandwidths on each day are the same and we measured $B_{2\sigma} = 75 \pm 15$ Hz from the weighted sum of all runs.

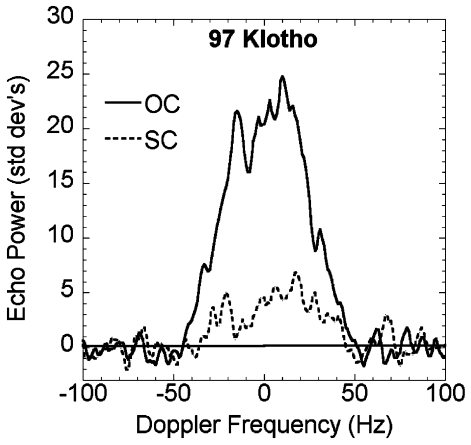

Fig. 8. Single CW spectrum of Klotho on 22 Dec 2006, smoothed to 5 Hz effective resolution.

Given that bandwidth and $P = 35.81$ h, we estimate $D_{\rm max} = 97 \pm 20$ km$/\cos\delta$, consistent with previous size estimates and indicative of an equatorial aspect. Our measured OC radar cross-section is $\sigma_{\rm OC} = 1020$ km^2, resulting in a radar albedo $\hat{\sigma}_{\rm OC} = 0.19 \pm 0.05$, more consistent with a mostly silicate chondritic body than a dominantly metallic one. We measured a polarization ratio $\mu_c = 0.22 \pm 0.05$, consistent with the mean for known S-class MBAs, 0.20 ± 0.09 (Magri et al., 2007a).

There have been reports of a possible satellite of Niobe based on a stellar occultation (Dunham, 2005, http://iota.jhuapl.edu/mp071.htm). We see no compelling evidence for a satellite in the radar data. However, the reported size (∼16 km) would result in an object with only 3% of Niobe's surface area. Assuming similar radar albedos, the SNR of our experiment makes it unlikely that we would detect such an object unless it was at least half the size of Niobe.

3.4. 97 Klotho

Klotho has IRAS diameter $D_{\rm eff} = 83 \pm 5$ km and visual albedo $p_v = 0.23 \pm 0.03$; it has a rotation period, $P = 35.15$ h (Tedesco et al., 2002; Lagerkvist et al., 1998). Tungalag et al. (2002) examined lightcurves from five oppositions between 1949 and 1994. They revised the period to $P = 35.11749 \pm 0.00001$ h, estimated ellipsoid axis ratios $a/b = 1.33 \pm 0.03$ and $b/c = 1.10 \pm 0.02$, and reported a pole position of $(\lambda, \beta) = (340° \pm 15°, 8° \pm 6°)$.

Magri et al. (1999) report two radar experiments with Klotho, the first in 1981 at Arecibo and the second at Goldstone ($\lambda = 3.5$ cm) in 1993–1994. The results of those two experiments were consistent with OC radar cross-sections of 1100 ± 310 km^2 and 1200 ± 320 km^2, respectively. Assuming $D_{\rm eff} = 83$ km, they report a radar albedo $\hat{\sigma}_{\rm OC} = 0.21 \pm 0.06$. The Arecibo experiment had a low SNR and the SC echo was not detected. The Goldstone estimate of polarization ratio is $\mu_c = 0.23 \pm 0.07$.

We observed Klotho on 2006 Dec 22 at a position $(\lambda, \beta) = (90°, -21°)$ (Table 3). Assuming the Tungalag et al. pole, our subradar latitude was $\delta = -21° \pm 10°$. Our single CW run had an SNR of 65 (Fig. 8, Table 4). We measured a bandwidth

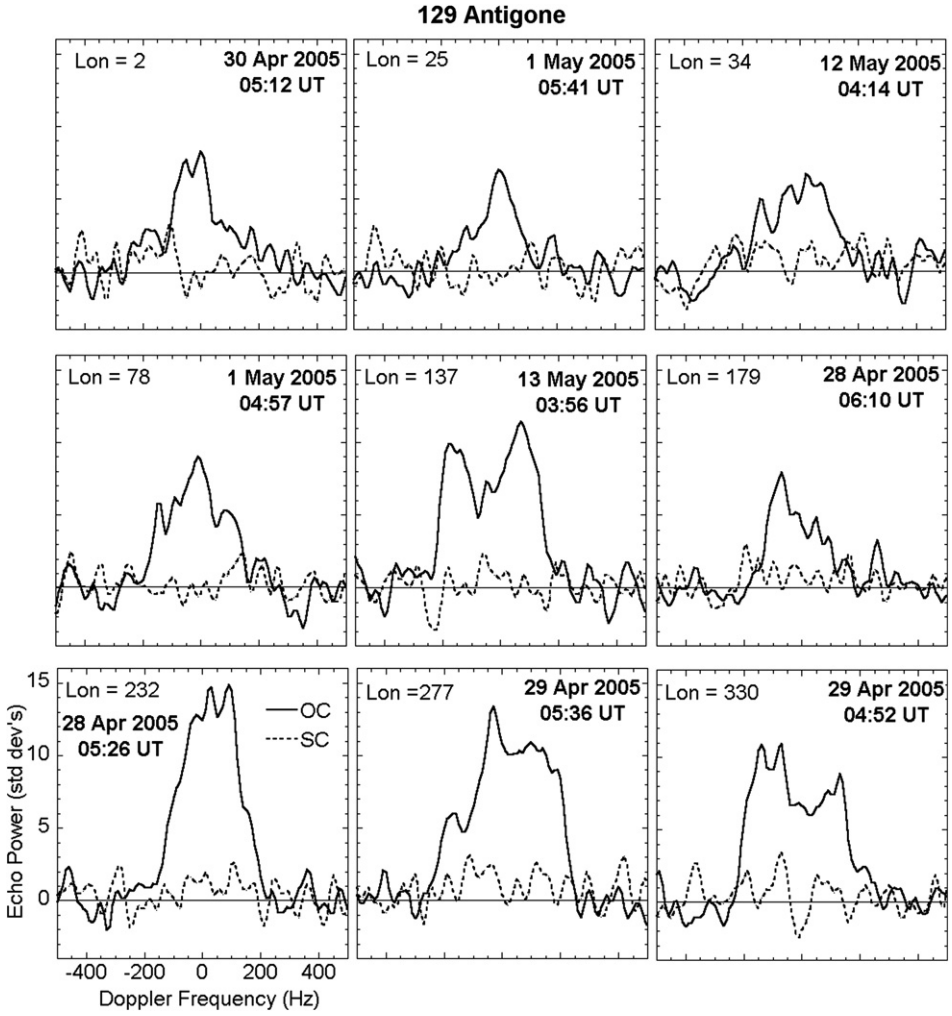

Fig. 9. CW data of Antigone. Longitudes based on shape model are shown in upper left; dates and times of radar acquisition are also indicated. The data have been smoothed to 40 Hz effective frequency resolution.

$B_{2\sigma} = 75 \pm 10$ Hz, an OC cross-section $\sigma_{OC} = 1420 \pm 350$ km^2, and a polarization ratio $\mu_c = 0.24 \pm 0.02$. Our radar cross-section is 25% higher than the previous estimates but within the 25% systematic uncertainties we typically assign. Our polarization ratio is consistent with previous Goldstone results. Given the aspect and including all uncertainties, we estimate $D_{max} = 101 \pm 20$ km (Eq. (2)). Assuming Tungalag et al.'s reported a/b elongation, our estimate of D_{max} is consistent with $D_{eff} = 83$ km if we observed one of the broader faces. Our assumed D_{eff} and observed radar cross-section lead to a radar albedo of 0.26 ± 0.05, higher than previous estimates but still within the systematic uncertainties. Nevertheless, this value exceeds our expectations for typical chondritic materials with bulk porosities of 50 ± 10%. It may be that the surface of Klotho has a lower porosity than assumed or that it contains a significant amount of metal. With the data we have, we are unable to resolve the question.

3.5. 129 Antigone

Antigone was not observed by IRAS, but at least two occultations have been reported that give effective diameters of 113–130 km and an associated visual albedo of ~0.18 (Wasserman et al., 1986; Dunham et al., 2002; Shevchenko and Tedesco, 2006). Using lightcurves from 13 apparitions, Torppa et al. (2003) estimate a shape and pole for Antigone. Their shape has axis ratios $a/b = 1.3$ and $b/c = 1.0$. They report a pole position of $(\lambda, \beta) = (207°, +58°) \pm 10°$, a sidereal rotation period $P = 4.957154 \pm 0.000005$ h, and evidence of albedo variegation. Rivkin et al. (2000) report the detection of a 3 μm feature attributed to water of hydration on Antigone and classify it as "W-class."

We observed Antigone on five nights in April and May 2005, obtaining nine runs with a total SNR of 60 (Tables 3, 4). Our measurements of radar cross-section on 28 Apr–1 May varied by a factor of three, so we requested and obtained additional observation time on 12–13 May (see Appendix A). These follow-up observations confirmed the large variations (Fig. 9, Table 4). The weighted sum of our CW observations have a $B_{2\sigma} = 440 \pm 20$ Hz; using the pole position reported by Torppa et al. (2003) and including the pole position uncertainties, we estimate $D_{max} = 130 \pm 30$ km. B_{EQ} varies significantly with rotation phase (Table 4), suggesting that Antigone has axis ratio a/b closer to 1.5 than to the previously reported value of

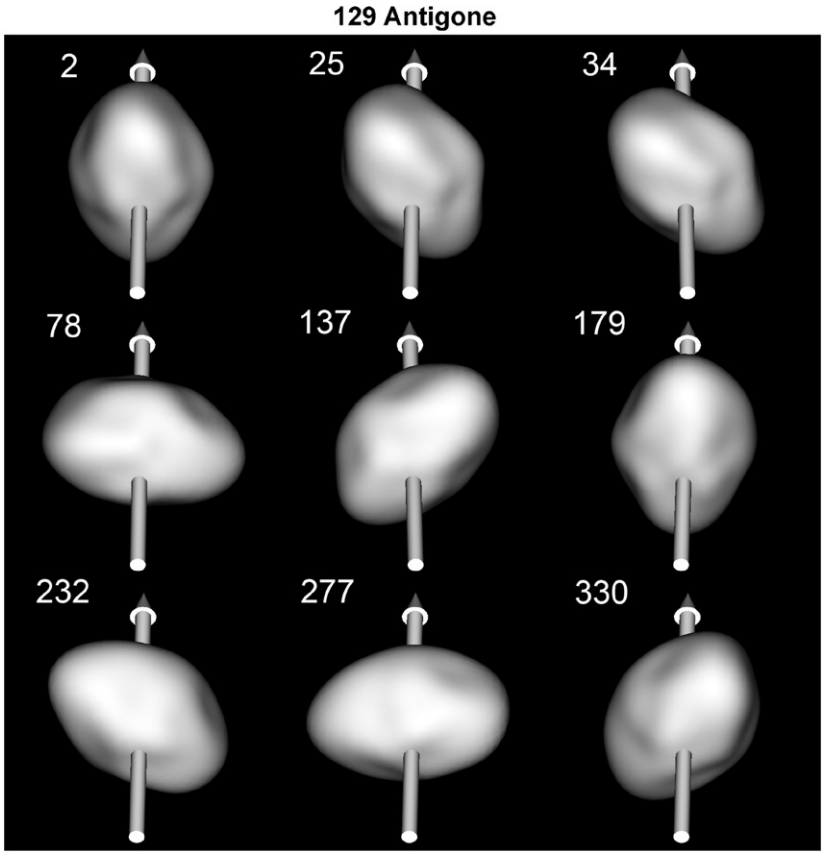

Fig. 10. Plane-of-sky rendering of Antigone at the radar acquisition times. Sub-radar longitudes are given in upper left. Arrows show the spin axis. The shading is Lambertian to emphasize the shape. Sub-observer longitude is 0° at JD 2453491.54415 (2005 May 01 01:03:34).

Table 6
Antigone shape model

Shape model parameters	
X: 152 km ±15%	
Y: 109 km ±15%	
Z: 95 km ±15%	
$a/b = 1.4 \pm 0.3$, $b/c = 1.2 \pm 0.2$	
$D_{\rm eff} = 113$ km ± 15%	
Area $= 4.2 \times 10^4$ km^2 ± 30%	
Volume $= 7.5 \times 10^5$ km^3 ± 50%	
Diameter of ellipsoid with equivalent volume	150 km × 101 km × 94 km

1.3 (Torppa et al., 2003). However, this aspect ratio is still insufficient to explain the large swings we observe in radar cross-section.

We generated a shape model using methods outlined by Hudson (1993) and most recently described in detail by Magri et al. (2007b). We adopted the Torppa et al. pole position and used our CW observations (10 Hz resolution) and lightcurves from the April 2005 (RB, http://obswww.unige.ch/~behrend/page1cou.html) and August 2006 (DP, this work) oppositions. Given this model, our radar observations are at subradar latitudes of $\delta = -51°$ and the lightcurves are at mid-southern (−48°, RB) and mid-northern (+38°, DP) latitudes. We assumed a homogeneous radar scattering law and allowed radar albedo to float. We began with ellipsoid models to check the aspect ratio reported by Torppa et al. and then fit an 8th order spherical harmonic shape to capture some of the variation observed in the CW data. Although there is some evidence for large concavities (central dips in the frequency spectrum at longitudes 137° and 330°), we decided to conservatively limit our models to be convex or nearly so. Our best solution is shown in Fig. 10 and described in Table 6. Principal axis views are shown in Fig. 11 and model fits to the CW data and lightcurves are shown in Figs. 12 and 13. Our model size, $D_{\rm eff} = 113 \pm 18$ km, is equal to the infrared diameter from the TRIAD file and the occultation diameter of Wasserman et al. (1986), and within uncertainties, consistent with the more recent occultation diameter of 130 km (Shevchenko and Tedesco, 2006). Our estimated visual albedo is $p_v = 0.21 \pm 0.05$.

If the radar and visual albedo are constant across the surface, we would expect them to be correlated with the projected area of the shape model at the time of their observations. Fig. 13 shows that the lightcurve can be well matched assuming a constant visual albedo. In Fig. 14, we normalized each run's radar cross-section to its projected area to estimate radar albedo. The superposed lightcurve serves as a proxy for projected area. This figure shows that much of Antigone has a high radar albedo of ∼0.4. However, the radar albedo at longitudes of 0°–90° is less than half this suggesting that this end is not as radar bright as the rest of the asteroid.

We used our shape model to extrapolate the viewing geometry to the 30 September 1996 3-μm observations of Rivkin et al. (2000) and found that they were acquired between longitudes 200°–240° and centered on latitude +20° (this extrapo-

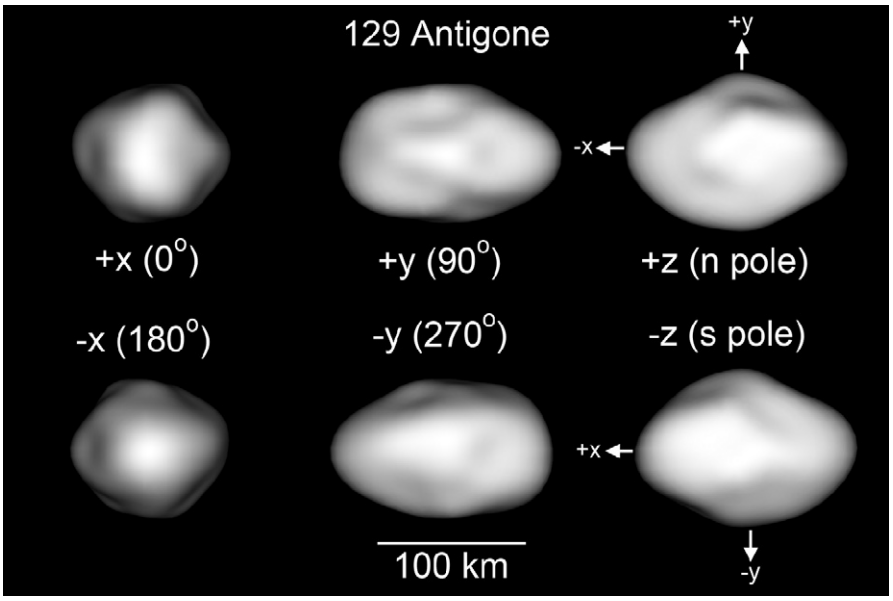

Fig. 11. Shape model of 129 Antigone as viewed from each end of the three principal axes. Aspects refer to axis and longitude pointing toward the viewer.

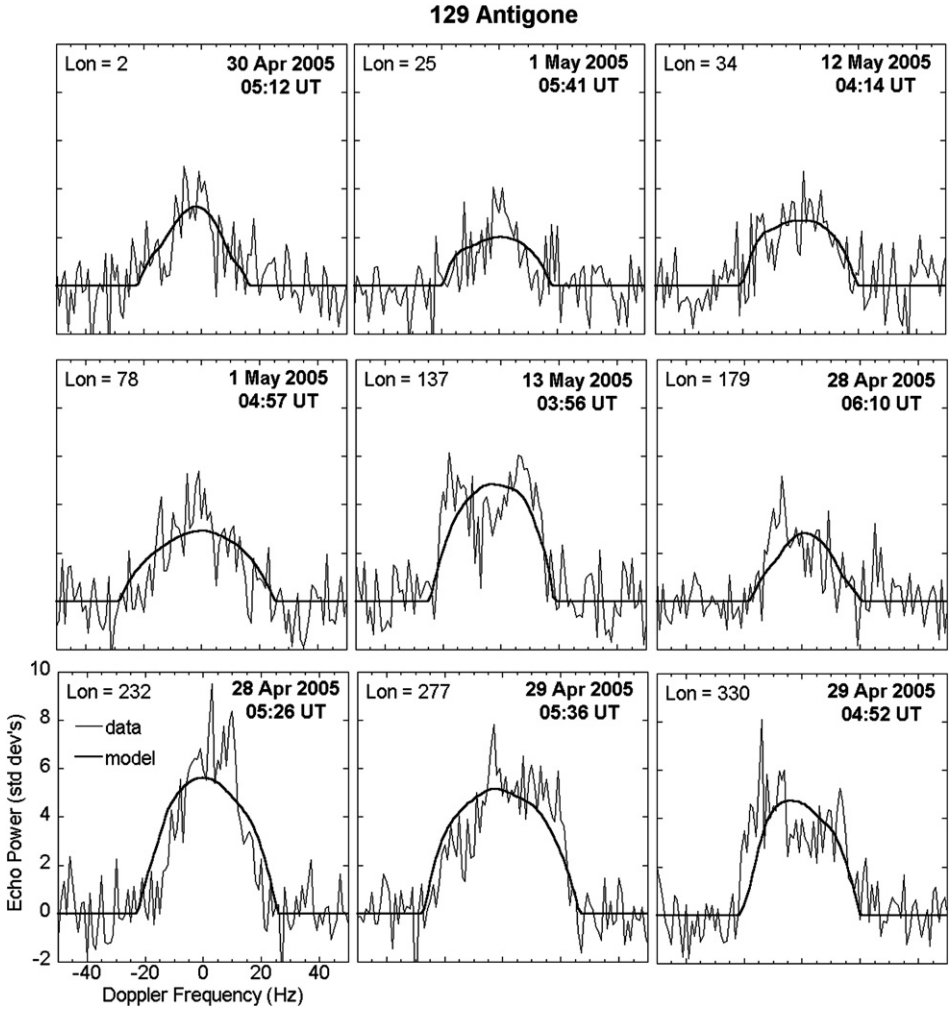

Fig. 12. Shape model fits to Antigone CW data. The data are at 10 Hz effective frequency resolution.

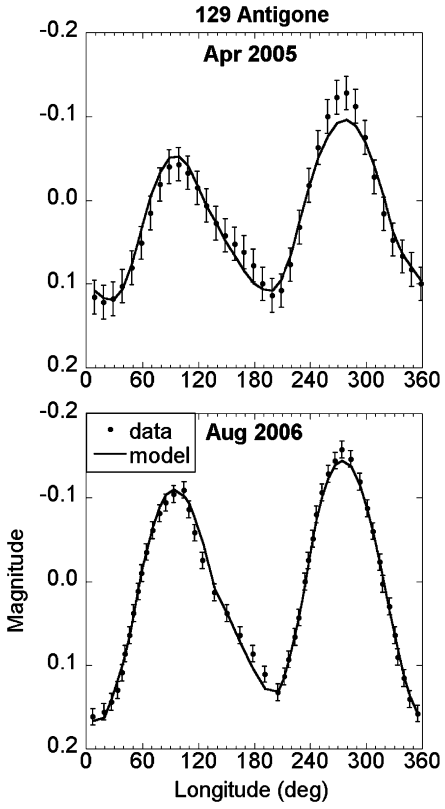

Fig. 13. Shape model fits to Antigone lightcurves (see text for sources).

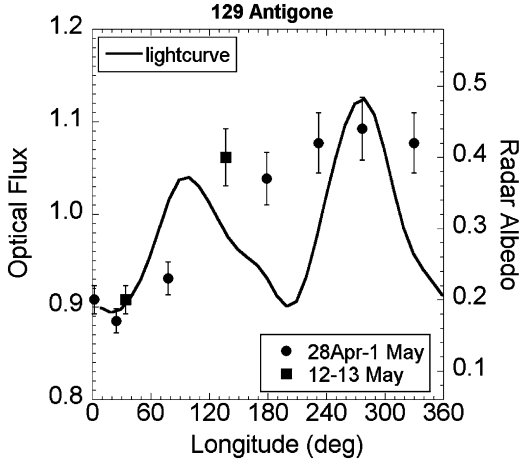

Fig. 14. Radar albedo of Antigone, normalized to the apparent geometric cross-section, superposed with its lightcurve. Lightcurve is in units of flux, a proxy for projected area. Uncertainties in radar albedo are 10%.

lation is valid if the period reported by Torppa et al. is within ±0.000010 h of the true period). This longitude is in the middle of our high radar albedo region but 70° north of our subradar latitude. Thus large areas of the northern hemisphere observed by Rivkin et al. were hidden to the radar.

Our maximum radar albedo is consistent with a near-surface comprised largely of metal with significant porosity, but the observed hydration feature makes this composition improbable. However, CH and CB meteorites, carbonaceous chondrites with high metal abundances, contain up to 20 and 60% metal by volume, respectively, and samples from both classes contain hydrated phases (Krot et al., 2002; Greshake et al., 2002). Greshake et al. (2002) argue that the existence of hydrated clasts within these otherwise anhydrous meteorites indicates that they experienced hydration in a different asteroidal setting and were later transported and incorporated into their current parent body.

What physical properties can explain the rotational variations observed in the radar albedo? One interpretation, consistent with the possible origin of CH and CB meteorites outlined above, is that the asteroid may be heterogeneous in composition, the result of a collision between a hydrous and anhydrous metal-rich asteroid. A second interpretation is that the asteroid is homogeneous in composition, perhaps metallic, but regolith thickness or porosity varies. A third interpretation is that Antigone does not have a significant metal content, and the high radar albedo region is likely devoid of significant regolith. This latter interpretation is counter to our initial assumptions and, while possible, is unlikely for a MBA.

Mueller et al. (2005) obtained thermal infrared observations in May 2005 at the Keck Observatory on Mauna Kea. We coordinated with them so that their observations were timed to observe longitudes ∼20° and ∼260° (latitudes −51°), thereby including regions of both high and low radar albedo. They report no observed variation in thermal emission. Ockert-Bell et al. (2008) obtained rotationally resolved spectra from the IRTF and found modest but inconsistent variations in the spectra. Given the evidence, especially the thermal observations, it is probably safe to rule out the 'bare rock' interpretation. Our polarization ratios vary significantly with rotation phase but do not appear to be correlated with radar albedo, effectively ruling out wavelength-scale surface roughness as the major cause of the albedo variations. We cannot rule out the collision between two disparate bodies because subsequent impacts and regolith gardening may result in only subtle spectral variations in the surface regolith. Nor can we rule out variations in regolith thickness or porosity variations with depth; these could affect the radar echo without influencing the spectral or thermal skin depths.

3.6. 135 Hertha

Hertha has an IRAS diameter of $D_{\rm eff} = 79 \pm 2$ km, visual albedo $p_v = 0.14 \pm 0.01$ (Tedesco et al., 2002), and period $P = 8.4006$ h (Torppa et al., 2003). Using lightcurves from eight apparitions, Torppa et al. (2003) derive a shape for Hertha with axis ratios $a/b = 1.1$ and $b/c = 1.5$ and report two possible poles: $(\lambda, \beta) = (135, +46)$ and $(310, +43)$. Hertha is one of larger members of the Nysa family and has been interpreted as the remnant core of a disrupted parent body which produced both Nysa (an E-class object) and Hertha (Zellner et al., 1977). Rivkin et al. (2000) observed a 3 μm absorption feature attributed to hydration and classified Hertha as a W, shedding some doubt on its interpretation as a remnant core. Additional work by Cellino et al. (2001) suggests that Hertha may be an interloper to this family and also argues against the remnant core interpretation.

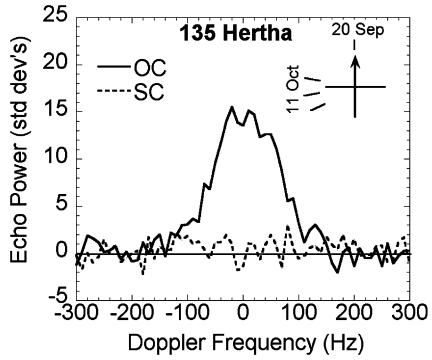

Fig. 15. Weighted sum of all CW runs of 135 Hertha. See Fig. 2 for a description of the rotation phase inset at upper right.

Table 7
Additional poles for 135 Hertha (see Cellino et al., 2003)

λ (°)	β (°)	δ (°)
106	+02	90
286	−02	90
118	+52	91
298	−52	89
291	+47	81
111	−47	99

We observed Hertha on two nights in September and October 2005, obtaining a total of four runs (Table 3). Individual and daily sums of our data are listed in Table 4. The optimally filtered sum of all spectra has a total SNR of 48 (Fig. 15). We estimate the bandwidth to be $B_{2\sigma} = 225 \pm 50$ Hz.

The reported diameter and period predict $B_{\rm obs} \leqslant 250$ Hz. Our observations are consistent with this and suggest a sub-radar latitude within a few tens of degrees of the equator. Several poles have been published for Hertha (Torppa et al., 2003; Table 7) and all are consistent with our data to within uncertainties.

Our OC radar cross-section estimate is $\sigma_{\rm OC} = 810 \pm 250$ km^2, giving an OC radar albedo $\hat{\sigma}_{\rm OC} = 0.18 \pm 0.06$, typical of the average MBA (see Table 6 in Magri et al., 2007a), and not indicative of a dominantly metallic surface. Hertha's polarization ratio is $\mu_c = 0.10 \pm 0.03$, suggesting a smooth surface at cm-to-m scales.

Our two days' observations were at rotation phases orthogonal to each other, and we plot these in Fig. 16. The total sky motion between these two dates was 5°, so there was little aspect change. Both days have statistically identical bandwidths suggesting a low a/b ratio, consistent with the Torppa et al. (2003) shape model. Although the 11 Oct spectrum is the sum of 3 runs, it is weaker than the single run on 20 Sep, suggesting a lower radar reflectivity on that side. Assuming similar projected areas, consistent with the similar bandwidths, we obtain nominal OC radar albedos of $\hat{\sigma}_{\rm OC} = 0.22$ and 0.14, respectively. There is also a difference in the daily polarization ratio estimates. We measured 0.02 ± 0.03 on 20 Sep and 0.13 ± 0.03 on 11 Oct. A larger polarization ratio indicates that more of the incident radar power is scattered diffusely rather than singly.

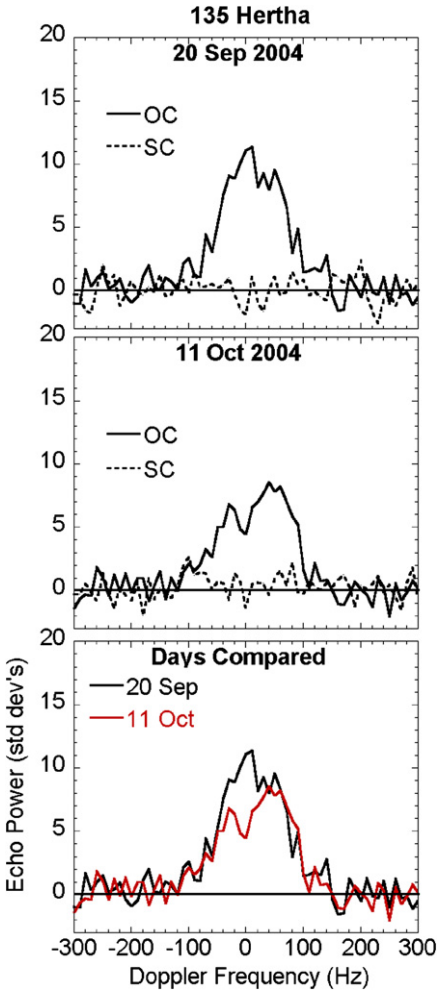

Fig. 16. Daily CW sums of Hertha compared.

Therefore, much, if not all of the difference in radar albedo is likely due to differences in near-surface roughness and not composition.

3.7. 224 Oceana

Little is known about Oceana. Its IRAS diameter is $D_{\rm eff} = 62 \pm 2$ km and its associated visual albedo is $p_v = 0.17 \pm 0.01$ (Tedesco et al., 2002). Oceana's period was tentatively reported to be $P = 18.933$ h or possibly half of that (Harris and Young, 1980, 1983). Because the rotation period was not well determined, Warner (2006) obtained lightcurve data over five nights in January 2006. Those data are consistent with periods of $P = 18.785 \pm 0.001$ h and 9.388 ± 0.001 h, and have an amplitude of 0.1 mag, suggesting an equant object or a near-polar aspect.

We observed Oceana on three nights in October, 2004, obtaining a total of four runs (Tables 3, 4). The optimally filtered sum of all spectra was folded about 0 Hz giving a total SNR of 12 (Fig. 17). We estimate the bandwidth to be $B_{\rm ZC} = 175 \pm 15$ Hz.

The IRAS diameter and $P = 18.785$ h requires a bandwidth $B_{\rm obs} \leqslant 90$ Hz. Since this is grossly inconsistent with our obser-

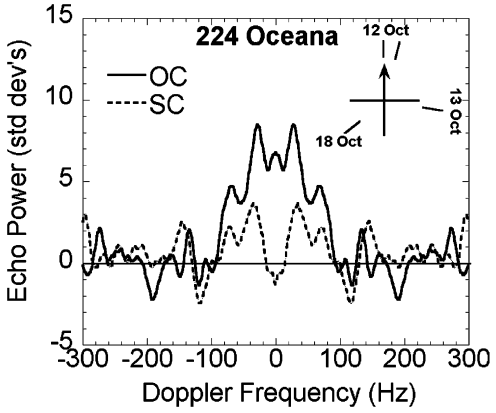

Fig. 17. Weighted sum of all CW runs of 224 Oceana. The spectrum has been folded about 0 Hz to boost SNR. See Fig. 2 for a description of the rotation phase inset at upper right.

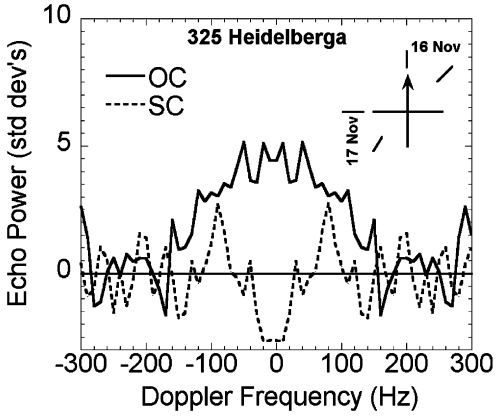

Fig. 18. Weighted sum of all CW runs of 325 Heidelberga. The spectrum has been folded about 0 Hz to boost SNR. See Fig. 2 for a description of the rotation phase inset at upper right.

vations, we rule out this period. Using a period of $P = 9.388$ h constrains $B_{\rm obs} \leqslant 180$ Hz. Our observations are consistent with this bandwidth and a subradar latitude within a few tens of degrees of the equator.

Our OC radar cross-section is $\sigma_{\rm OC} = 750 \pm 300$ km^2 giving an OC radar albedo $\hat{\sigma}_{\rm OC} = 0.25 \pm 0.10$. Like Klotho, this value is higher than expected for typical chondritic materials with bulk densities of $50 \pm 10\%$ and we cannot rule out a significant metal content, especially at the upper end of our uncertainties. Oceana's polarization ratio, $\mu_c = 0.33 \pm 0.06$, is higher than that of most MBAs and is indicative of a rough near-surface at cm-to-m scales.

3.8. 325 Heidelberga

Heidelberga's IRAS diameter is $D_{\rm eff} = 76 \pm 2$ km and its associated visual magnitude is $p_v = 0.11 \pm 0.01$ (Tedesco et al., 2002). Its rotation period is $P = 6.7366 \pm 0.0006$ h (Harris et al., 1992). No pole has been published for it.

We observed Heidelberga on two nights on 16–17 November, 2005, obtaining a total of four runs (Tables 3, 4). Because of the low SNR, we folded our summed spectrum about 0 Hz resulting in a SNR of 14 (Fig. 18). We estimate the bandwidth to be $B_{\rm ZC} = 270 \pm 30$ Hz. Heidelberga's polarization ratio is $\mu_c = 0.0 \pm 0.1$, which is unusually low and consistent with a very smooth surface at the cm-to-m scale.

Assuming the IRAS diameter to be the longest axis, $D_{\rm max}$, we predict $B_{\rm obs} \leqslant 310$ Hz. Our observations are consistent with this prediction and subradar latitudes of $\delta = 0°$–$40°$. Our OC radar cross-section is $\sigma_{\rm OC} = 775 \pm 400$ km^2 giving an OC radar albedo of $\hat{\sigma}_{\rm OC} = 0.17 \pm 0.08$. This is similar to the average radar cross-section for MBAs and is inconsistent with a metallic composition for reasonable near-surface porosities.

3.9. 758 Mancunia

Mancunia was an X-class in the Tholen (1984) taxonomy, but its visual albedo $p_v = 0.13 \pm 0.02$ (Tedesco et al., 2002) places it in the M-category. Its IRAS diameter is $D_{\rm eff} = 85 \pm 7$ km (Tedesco et al., 2002) and Holliday (1996) reports a rotation period of 6.902 ± 0.004 h. Rivkin et al. (2000) did not detect a 3 μm hydration feature on Mancunia. No pole has been published.

We observed Mancunia on 21–23 Dec 2006 and obtained five runs with a total SNR near 40 (Tables 3 and 4, Fig. 19). Our observations, especially the similarity of runs #3 and #5, suggested that the reported rotation period was in error so we requested photometric observations from astronomers over the next few evenings. These observations cover a complete rotation period and give $P = 12.738 \pm 0.003$ h and a lightcurve amplitude of 0.26 ± 0.02 mag (Warner et al., 2008).

We estimate Mancunia's bandwidth to be $B_{2\sigma} = 207 \pm 20$ Hz giving $D_{\rm max} \geqslant 92$ km, which is consistent with the IRAS diameter if the aspect was nearly equatorial. We measured an OC radar cross-section of $\sigma_{\rm OC} = 3250 \pm 800$ km^2, leading to a radar albedo estimate of $\hat{\sigma}_{\rm OC} = 0.55 \pm 0.14$ (assuming $D_{\rm eff} = 85$ km), one of the highest values measured and one comparable to that of 216 Kleopatra (Ostro et al., 2000). We measured a polarization ratio $\mu_c = 0.34 \pm 0.03$ which is higher than 90% of radar detected main-belt asteroids and one of the highest for radar detected M-class asteroids (Magri et al., 2007a). $B_{2\sigma}$ varies from 162–215 Hz; if this represents the extremes in apparent breadth, it suggests an apparent axis ratio of $\sim$1.3 which is consistent with the lightcurve amplitude.

The central dips in echo power of radar runs #2 and #4 (Fig. 19) strongly suggest that Mancunia has significant concavities on opposite sides. These runs also have high polarization ratios of $\mu_c \sim 0.4$, consistent with very rough terrain, a thick inhomogeneous regolith, or both.

We found both radar cross-section and polarization ratio to vary considerably with rotation phase (Table 4, Fig. 20); $\sigma_{\rm OC}$ varies by a factor of 1.6 and μ_c varies by a factor of $\sim$2. Both show little correlation with the lightcurve flux, a proxy for projected area, suggesting the variations are not related to the gross shape. The OC cross-section and polarization ratio are strongly anti-correlated (Fig. 20), suggesting most of the variation in OC radar albedo is due to variations in regolith depth, porosity, or near-surface roughness.

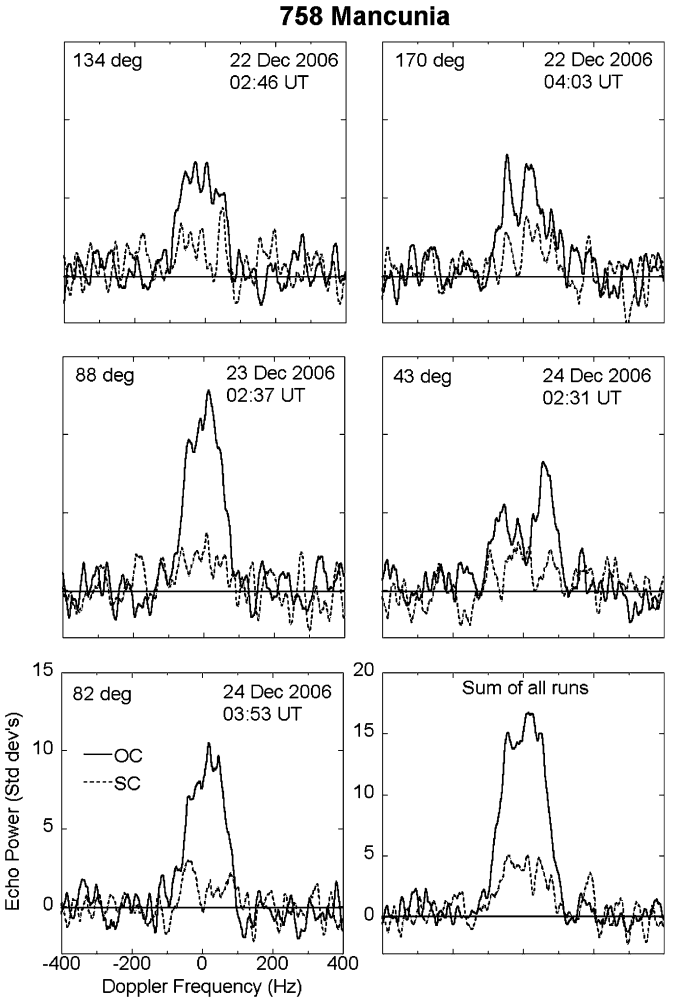

Fig. 19. CW data for 758 Mancunia. Plots are in chronological (run) order, left to right, top to bottom. All data have been smoothed to 20 Hz effective frequency resolution. Numbers at the top of each plot are rotation phase relative epoch JD 2454093.53 (2006 Dec 24 0:43:12 UTC). The plot at bottom right is the sum of all runs (note the larger vertical scale for this plot).

3.10. 785 Zwetana

Zwetana has an IRAS diameter of $D_{\rm eff} = 49 \pm 2$ km, visual magnitude $p_v = 0.12 \pm 0.01$ (Tedesco et al., 2002), and a reported rotational period of $P = 8.9$ h (Dotto et al., 1992). Rivkin et al. (1995) report no observed 3 μm hydration feature in its spectrum. No pole has been published for it.

We observed Zwetana on five nights in April and May 2005, obtaining a total of 13 runs with a total SNR of 44 (Tables 3 and 4, Fig. 21). Our observations on 28 Apr–1 May showed a factor of six variation in OC radar cross-section; because of this, we requested and obtained additional observation time on 12–13 May (see Appendix A). Our follow-up radar observations confirmed the large variations (Table 4). At the same time, we (MF, TB, AK, RB, HC, JC, SC) measured its lightcurve over five nights to confirm its period and estimate its lightcurve amplitude. Our data are consistent with a period of 8.8882 ± 0.0002 h and amplitude of 0.2, suggesting either a nearly-equant object or polar aspect.

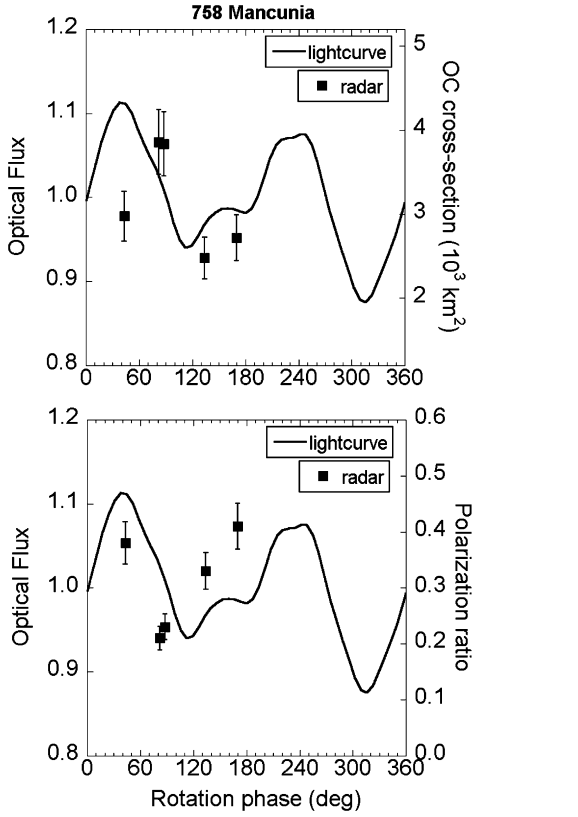

Fig. 20. Mancunia lightcurve at epoch of radar observations (see Fig. 19), OC cross-section, and polarization ratio. Uncertainties in OC cross-section are 10%; uncertainties in polarization ratio are give in Table 4.

We estimate $B_{2\sigma} = 160 \pm 20$ Hz from the weighted sum of all observations (Fig. 21). The IRAS diameter of 49 km and $P = 8.8882$ h predict a $B_{\rm obs} \leqslant 151$ Hz. Our lightcurve and radar data are therefore consistent with a nearly-equant object viewed within a few degrees of its equator, effectively ruling out a shape-related cause of the large swings in radar cross-section. We measured an overall radar cross-section of 615 ± 150 km^2 and a polarization ratio $\mu_c = 0.17 \pm 0.03$. The polarization ratio showed little variation except when SNR was <10. While this may be spurious, it could indicate that the near-surface at those rotation phases is rougher or more heterogeneous. This would also be consistent with the lower OC radar cross-section at those phases.

To investigate the variations in cross-section further, we normalized Zwetana's radar albedo to projected area by modeling it as an ellipsoid with axes 57 × 46 × 45 km, giving $D_{\rm eff} = 49$ km, axis ratios of $a/b = 1.2$ and $b/c = 1.0$, and an equatorial aspect (we did not generate a shape model because there is no reported pole). We set the a-axis to be 0° rotation phase, so that we see the broadest aspects at 90° and 270°, consistent with the lightcurve. Fig. 22 shows that Zwetana has a radar albedo as high as 0.6 at rotation phase 240°, consistent with a near-surface comprised largely of metal and similar to that observed for Kleopatra (Ostro et al., 2000) and Mancunia. However, the radar albedo at rotation phase 320° drops to 0.1, similar to that observed from more primitive asteroids (B-, F-, G-, and P-classes, Magri et al., 1999). The pattern of

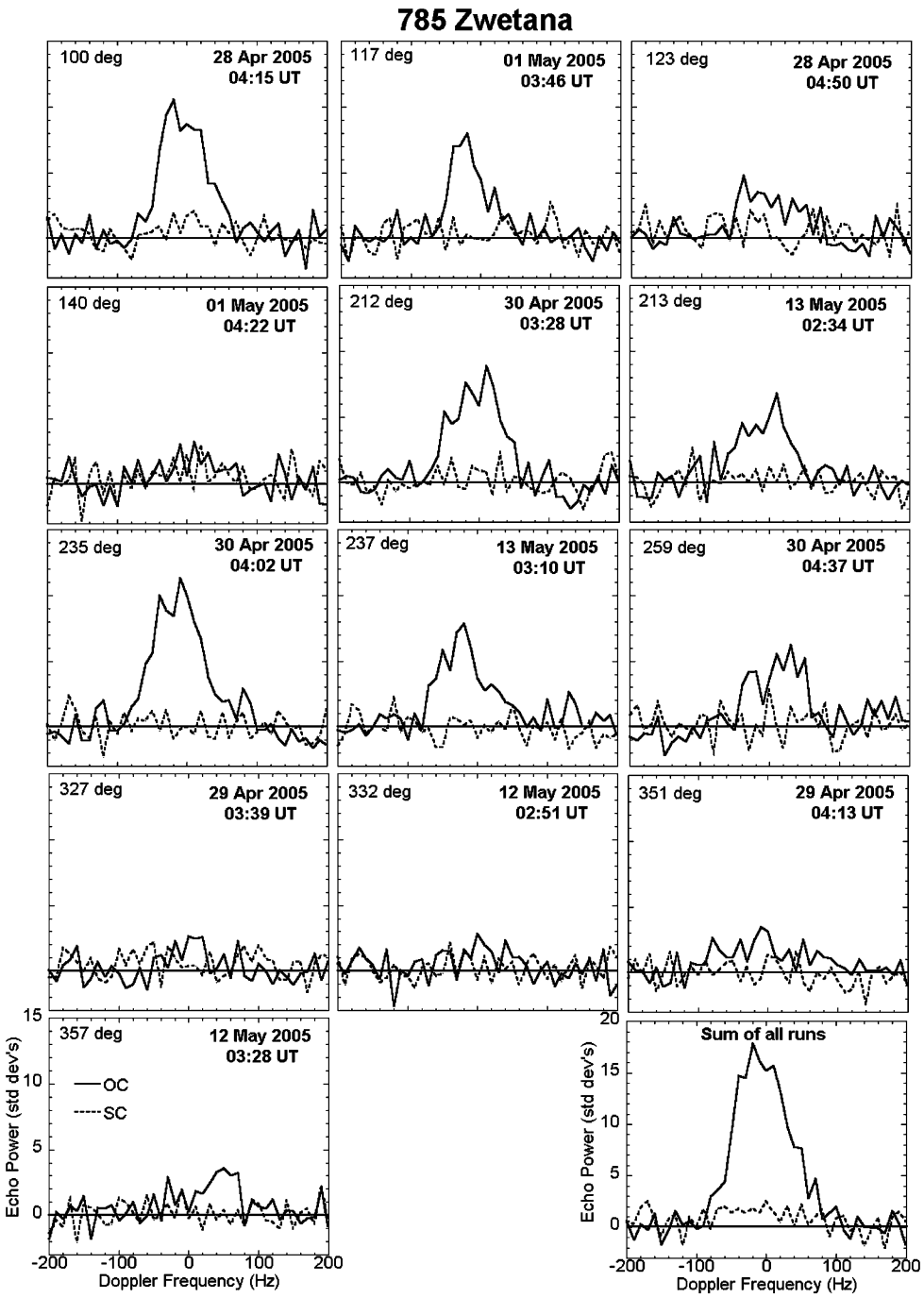

Fig. 21. CW spectra of 785 Zwetana, arranged in order of rotation phase, left to right and then top to bottom (epoch JD 2453494.49350, 1 May 2005). Figure at bottom right is the weighted sum of all runs. Frequency resolution is 10 Hz.

the radar albedo mimics the lightcurve and suggests that the two broader faces of Zwetana have high albedos while the two narrower ends have low albedos. If the radar albedo variations were due to shape alone, we would expect this normalization to bring all radar albedos closer together. Instead, we see the opposite.

There are at least three possibilities for the anomalous radar behavior. The broadsides may be of a different composition from the ends, perhaps a remnant of a collision with a different type of asteroid or a mantle fragment remaining after a disruptive collision. While possible, this option seems unlikely to explain the nearly perfect 180° symmetry of the highs and lows of radar albedo. To test this hypothesis, F. DeMeo and R. Binzel observed Zwetana at the IRTF immediately after our observations at numerous rotation phases covering different radar albedos and observed 1% or less spectral variation (Ockert-Bell et al., 2008). Similarly, Mueller et al. (2005) observed Zwetana at the Keck Observatory in JHK wavelengths at aspects corresponding to high and low radar albedos and observed no variation. In sum, spectral observa-

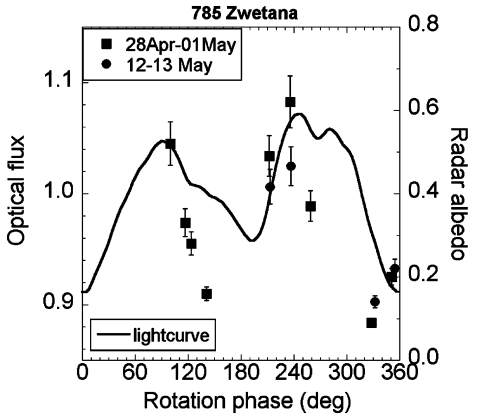

Fig. 22. Radar albedo of Zwetana, corrected for our model ellipsoid shape, as a function of rotation phase and superposed on our lightcurve. Uncertainties in radar albedo are 10%. Lightcurve epoch JD 2453494.49350, 2005 May 3 23:50:38.

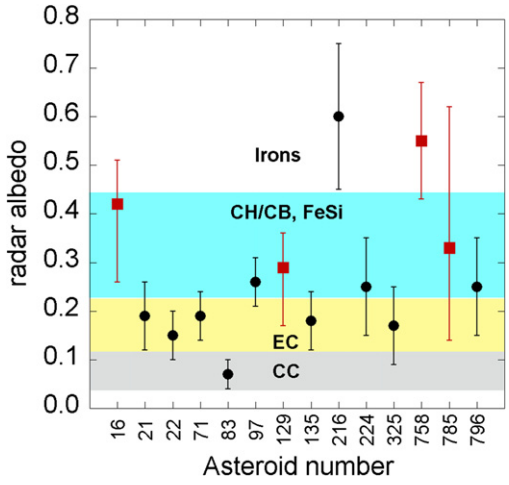

Fig. 23. Radar albedo for every M-class target observed by radar. Colored regions show range of radar albedos expected for compositional analogs listed in Table 2: gray is carbonaceous chondritic (CC), yellow is enstatite chondritic (EC), blue is CH/CB/Bencubbinite or Si-bearing irons (CH/CB, FeSi), and white (>0.43) is dominantly metallic (irons). Black circles are asteroids that show little or no variability or were not observed as part of this study. Absolute uncertainties shown for these are 25%. Red squares are asteroids in this study which (1) show significant variability with rotation phase and (2) appear to have a significant metallic component. Uncertainties for these show the *total range* of radar albedos observed for them with rotation. Uncertainties could shift the red points up or down by 25%, but this is not shown for clarity.

tions appear to rule out significant compositional variations on Zwetana.

Alternatively, the regolith on the two ends may be thicker or more porous resulting in a decreased reflectivity. However, this hypothesis requires an exceptionally high near-surface porosity of 70–80% for metallic compositions (see Fig. 3 of Ostro et al., 1985). One way around this somewhat unrealistic scenario is if the bulk density increases (or porosity decreases) with depth, essentially creating an impedance match between free space and the surface regolith which acts to absorb the radar (Simpson, 1976). Significant increases in bulk density have been documented in the uppermost meter of the lunar regolith (Table 9.5 of Carrier et al., 1991). However, the gravitational regime on Zwetana is very different from that on the Moon and the comparison may not be valid.

A third possibility is that Zwetana has a typical MBA radar albedo, but has at least two smooth global-scale facets oriented such that we receive unexpectedly large backscatter echoes, or glints, as it rotates. This hypothesis also explains why the radar albedo varies so rapidly with rotation, from radar bright to dark after only 30° of rotation. This hypothesis can be tested when Zwetana is visible at Arecibo again in 2009. It will be ∼25° away from the 2005 position and any facets may be less favorably oriented for backscattering; if so, our radar albedo should be low and not vary significantly with rotation.

4. Discussion

We now have observations of 14 MX-class MBAs, listed in Table 8 and plotted in Fig. 23. Of these, Psyche, Kleopatra, Mancunia, and Zwetana show strong evidence for a metallic composition. Thus about one-third of our M sample is demonstrably metallic. Of the Rivkin et al. (2000) 'non-hydrated' or M-class asteroids observed by radar, all appear to be dominated by metal, with the possible exception of 796 Sarita. Of the Rivkin et al. (2000) 'hydrated' or W-class asteroids observed with radar, all appear to have radar albedos typical of other MBAs with the exception of 129 Antigone. Its radar albedo may be consistent with a metallic composition, but is significantly lower than the other four. One possible interpretation is that Antigone is a CH/CB meteorite analog. Asteroids 97 Klotho, 224 Oceana, and 796 Sarita have nominal radar albedos that suggest a relatively high surface bulk density; this could result from a lower porosity than assumed here ($50 \pm 10\%$) or a higher than normal metal content.

Our observations of Psyche, Antigone, Mancunia, and Zwetana show these high radar-albedo objects to be more complex than originally suspected. All four exhibit significant rotational variations in radar albedo. (Hertha shows modest radar albedo variations with rotation, but it does not appear to be metallic.) The cause of these variations does not appear to be compositional with the possible exception of Antigone; even there the spectral variations are small and not consistent with the radar variations (Ockert-Bell et al., 2008). Thermal data from Antigone and Zwetana likewise show no rotational variation, but it must be remembered that the optical skin depth is a few micrometers, the thermal skin depth is on the order of millimeters to a few centimeters, and the radar depth is a few tens of centimeters. A thin global layer of homogeneous dust could mask underlying compositional variations from both spectral and thermal instruments.

The most likely causes of non-compositional variations in radar albedo are shape and surface texture or porosity. Psyche has long been suspected of an unusual shape based on its lightcurves, but it does not appear to be highly elongate, either in our radar data or previous lightcurves (see convex shape model of Kaasalainen et al., 2002). It appears to have a radar anomaly on only one side which may coincide with the reported optical bright spot reported by previous observers. The variations in Mancunia's radar albedo are anti-correlated with varia-

Table 8
Summary of physical and radar properties of M- and suspected M-class asteroids

Asteroid	D (km)	p_v	P (h)	$\hat{\sigma}_{OC}$	Metal	Var	μ_c	Tholen	Bus	Barucci	Rivkin
16 Psyche	186 ± 30	0.23 ± 0.05	4.196	0.42 ± 0.10	Y	Y	0.06 ± 0.02	M	X	M0	M
21 Lutetia	100 ± 11	0.20 ± 0.03	8.172	0.24 ± 0.07			0.22 ± 0.05	M	Xk	M0	W
22 Kalliope	181 ± 5	0.14 ± 0.01	4.148	0.15 ± 0.05			0.07 ± 0.10	M	X	M0	W
71 Niobe	83 ± 2	0.31 ± 0.01	35.81*	0.19 ± 0.05			0.22 ± 0.05	S	Xe	S0	
83 Beatrix	81 ± 2	0.09 ± 0.01	10.16	0.07 ± 0.03			0.23 ± 0.11	X	X	M0	
97 Klotho	83 ± 5	0.23 ± 0.03	35.15	0.26 ± 0.05	?		0.24 ± 0.02	M		M0	
129 Antigone	113 ± 12	0.21 ± 0.05	4.957	0.36 ± 0.09	?	Y	0.14 ± 0.02	M	X		W
135 Hertha	79 ± 2	0.14 ± 0.01	8.401	0.18 ± 0.06		Y	0.10 ± 0.03	M	Xk	M0	W
216 Kleopatra	124 ± 15	0.12 ± 0.02	5.385	0.60 ± 0.15	Y		0.00 ± 0.04	M	Xe	M0	M
224 Oceana	62 ± 2	0.17 ± 0.01	9.388*	0.25 ± 0.10	?		0.33 ± 0.06	M			
325 Heidelberga	76 ± 2	0.11 ± 0.01	6.737	0.17 ± 0.08			0.0 ± 0.1	M			
758 Mancunia	85 ± 7	0.13 ± 0.02	12.738*	0.55 ± 0.14	Y	Y	0.34 ± 0.03	X			M
785 Zwetana	49 ± 2	0.12 ± 0.01	8.919	0.33 ± 0.08	Y	Y	0.17 ± 0.03	M	Cb	B2	M
796 Sarita	45 ± 2	0.20 ± 0.01	7.75	0.25 ± 0.10	?		–	XD	X		M

D is asteroid effective diameter, p_v is visual albedo, P is rotation period, and asterisks indicate significant revisions to previously reported periods based on this work. $\hat{\sigma}_{OC}$ is radar albedo, metal indicates whether the asteroid is metallic (Y = yes, blank = no, ? = possible), Var indicates whether the asteroid shows variations in radar albedo with rotation (Y = yes, blank is no or unknown), μ_c is polarization ratio. The classifications listed are based on the following references: Tholen (Tholen, 1984), Bus (Bus and Binzel, 2002), Barucci (Barucci et al., 1987), and Rivkin (Rivkin et al., 2000). Uncertainties are listed for all quantities except period, which is on the order of the last significant digit unless otherwise stated in the text. Diameters and visual albedos are primarily from the IRAS data set (Tedesco et al., 2002) except where modified by our or previous radar data (see text for specific references).

tions in polarization ratio, suggesting near-surface roughness as a likely cause—perhaps related to concavities that appear in the CW waveforms. Antigone does not show evidence of unusual shape, although there is some evidence for significant concavities, leaving surface texture or porosity as the most likely cause of its observed variations. Zwetana also does not appear to be elongate and shows extreme variations in radar albedo. We see no compositional changes and it does not appear to be elongate. Possible causes for its variations include large variations in surface porosity and global-scale facets that were favorably aligned for backscatter during our observations.

5. Future observing opportunities

Of the targets described in this paper, we find the following future opportunities for radar observations at Arecibo. Psyche is next visible in December 2010 at SNRs of ∼20/day, comparable to those described here. Lutetia will be a modest CW target in November 2008 with SNRs of ∼25/day. Niobe will not present a targeting opportunity again until February 2015. Klotho will be a strong CW target and a possible imaging target in February 2016 with SNRs of ∼50/day. Antigone will not have a significant targeting opportunity again until Mar 2029; even then it will be only 70% as bright as the apparition noted in this paper. Hertha will be a potential target again in October 2008, but only at about half the SNR of that in this paper. Oceana will not have a targeting opportunity comparable to the last one until February 2015. There are no good opportunities to detect Heidelberga again for at least 25 years. We cannot target Mancunia again at SNRs comparable to those describe here until November 2023. Zwetana will be a target at SNRs comparable to those described here in March 2009.

X- and M-class asteroids in our future targeting list (through 2009) include 110 Lydia, 136 Austria, 261 Prymno, 322 Phaeo, 347 Pariana, 413 Edburga, 497 Iva, 572 Rebekka, 678 Fredegundis, 757 Portlandia, 771 Libera, and 779 Nina.

Acknowledgments

M.K.S. and B.E.C. gratefully acknowledge support from NSF Grants AST-0605903 and AST-0606704. C.M. was partially supported by NSF Grant AST-0205975. A.W.H. and B.D.W acknowledge support from NASA Grant NNG06GI32G and NSF Grant AST-0607505. P.P. was supported by the Grant Agency of the Czech Republic, Grant 205/05/0604. The Arecibo Observatory is part of the National Astronomy and Ionosphere Center, which is operated by Cornell University under a cooperative agreement with the National Science Foundation. We thank the technical staff at each observatory for help with observations. Some of this work was performed at the Jet Propulsion Laboratory, California Institute of Technology, under contract with the National Aeronautics and Space Administration. This material is based in part upon work supported by the National Aeronautics and Space Administration (NASA) under the Science Mission Directorate Research and Analysis Programs.

Appendix A

785 Zwetana and 129 Antigone were observed in April–May, 2004 during the same observation window. Both showed large variations in radar cross-section which were immediately suspected to be due to unknown instrument-based factors. Here, we list the facts which suggest that the variations were real.

1. No anomalies were reported with the system before or after our runs.
2. We observed 2 Pallas on three nights at the beginning of our Zwetana and Antigone runs. Our results were constant

from night-to-night and consistent with previous radar observations of Pallas (Mitchell et al., 1996).

3. Our observations show no systematic pattern in time. On two nights, both asteroids have moderate to high radar cross-sections; on two, both have moderate to low cross-sections; and on two nights, one asteroid has a high cross-section while the other is low.
4. Repeat observations on 12–13 May were consistent with predictions based on the known rotation period of both asteroids.

References

Baer, J., Chesley, S.R., 2008. Astrometric masses of 21 asteroids, and an integrated asteroid ephemeris. Celest. Mech. Dynam. Astron. 100, 27–42.

Barruci, M.A., Capria, M.T., Coradini, A., Fulchignoni, M., 1987. Classification of asteroids using G-mode analysis. Icarus 72, 304–324.

Bell, J.F., Davis, D.R., Hartmann, W.K., Gaffey, M.J., 1989. Asteroids: The big picture. In: Binzel, R.P., Gehrels, T., Matthews, M.S. (Eds.), Asteroids II. Univ. of Arizona, Tucson, pp. 921–948.

Binzel, R.P., Bus, S.J., Xu, S., Sunshine, J., Burbine, T.H., 1995. Rotationally resolved spectra of Asteroid 16 Psyche. Icarus 117, 443–445.

Britt, D.T., Yeomans, D., Housen, K., Consolmagno, G., 2002. Asteroid density, porosity, and structure. In: Bottke Jr., W.F., Cellino, A., Paolicchi, P., Binzel, R.P. (Eds.), Asteroids III. Univ. of Arizona, Tucson, pp. 485–500.

Bus, S.J., Binzel, R.P., 2002. Phase II of the Small Main-Belt Asteroid Spectroscopic Survey: A feature-based taxonomy. Icarus 158, 146–177.

Campbell, D.B., Davis, M.M., Goldsmith, P.F., Perillat, P.J., 1997. The new Arecibo telescope: Status and performance. Bull. Am. Astron. Soc. 29. Abstract 1305.

Carrier III, W.D., Olhoeft, G.R., Mendell, W., 1991. Physical properties of the lunar surface. In: Heiken, G.W., Vaniman, D.T., French, B.M. (Eds.), Lunar Sourcebook: A User's Guide to the Moon. Cambridge Univ. Press, New York, pp. 475–594.

Cellino, A., Zappala, V., Doressoundiram, A., Di Martino, M., Bendjoya, Ph., Dotto, E., Migliorini, F., 2001. The puzzling case of the Nysa-Polana family. Icarus 152, 225–237.

Cellino, A., Diolaiti, E., Ragazzoni, R., Hestroffer, D., Tanga, P., Ghedina, A., 2003. Speckle interferometry observations of asteroids at TNG. Icarus 162, 278–284.

Clark, B.E., Bus, S.J., Rivkin, A.S., McConnochie, T., Sanders, J., Shah, S., Hiroi, T., Shepard, M., 2004. E-type asteriod spectroscopy and compositional modeling. J. Geophys. Res 103. E02001.

Cloutis, E.A., Gaffey, M.J., Smith, D.G.W., Lambert, R.St.J., 1990. Metal silicate mixtures: Spectral properties and applications to asteroid taxonomy. J. Geophys. Res. 95, 8323–8338.

Dotto, E., Barucci, M.A., Fulchignoni, M., Di Martino, M., Rotundi, A., Burchi, R., Di Paolantonio, A., 1992. Astron. Astrophys. Suppl. Ser. 95, 195–211.

Drummond, J.D., Christou, J., 2006. Sizing up asteroids at Lick Observatory with adaptive optics. Bull. Am. Astron. Soc. 38. Abstract 59.25.

Dunham, D.W., Goffin, E., Manek, J., Federspiel, M., Stone, R., Owen, W., 2002. Asteroidal occultation results multiply helped by HIPPARCOS. Mem. Soc. Astron. Ital. (J. Ital. Astron. Soc.) 73, 662–665.

Fanale, F.P., Johnson, T.V., Matson, D.L, 1974. Io's surface and the histories of the Galilean satellites. In: Burns, J. (Ed.), Planetary Satellites. Univ. of Arizona Press, Tucson, pp. 378–408.

Fulchignoni, M., Barucci, M.A., Fornasier, S., Dotto, E., Vernazza, P., Birlan, M., Carvano, J., Merln, F., Belskaya, I., 2004. 2867 Steins and 21 Lutetia: The Rosetta mission asteroid targets, Bull. Am. Astron. Soc. 36. Abstract 28.03.

Gaffey, M.J., 1976. Spectral reflectance characteristics of the meteorite classes. J. Geophys. Res. 81, 905–920.

Gaffey, M.J., Burbine, T.H., Binzel, R.P., 1993. Asteroid spectroscopy: Progress and perspectives. Meteoritics 28, 161–187.

Greshake, A., Krot, A.N., Meibom, A., Weisberg, M.K., Zolensky, M.E., Keil, K., 2002. Heavily-hydrated lithic clasts in CH chondrites and the related metal-rich chondrites Queen Alexandra Range 94411 and Hammadah al Hamra 237. Meteorit. Planet. Sci. 37, 281–293.

Hardersen, P.S., Gaffey, M.J., Abell, P.A., 2002. M-asteroids: Searching for weak silicate features on potentially differentiated objects. Lunar Planet. Sci. 33. Abstract 1148.

Harris, A.W., Young, J.W., 1980. Asteroid rotation. III. 1978 Observations. Icarus 43, 20–32.

Harris, A.W., Young, J.W., 1983. Asteroid rotation. IV. 1979 Observations. Icarus 54, 59–109.

Harris, A.W., Young, J.W., 1989. Asteroid lightcurve observations from 1979–1981. Icarus 81, 314–364.

Harris, A.W., Young, J.W., Dockweiler, T., Gibson, J., Poutanen, M., Bowell, E., 1992. Asteroid lightcurve observations from 1981. Icarus 95, 115–147.

Holliday, B., 1996. Photometric observations of minor planet 758 Mancunia. Minor Planet Bull. 23, 28.

Hudson, S., 1993. Three-dimensional reconstruction of asteroids from radar observations. Remote Sens. Rev. 8, 195–203.

Johnson, T.V., Fanale, F.P., 1973. Optical properties of carbonaceous chondrites and their relationship to asteroids. J. Geophys. Res. 78, 8507–8518.

Jones, T.D., Lebofsky, L.A., Lewis, J.S., Marley, M.S., 1990. The composition and origin of the C, P, and D asteroids: Water as a tracer of thermal evolution in the outer belt. Icarus 88, 172–192.

Kaasalainen, M., Torppa, J., Piironen, J., 2002. Models of twenty asteroids from photometric data. Icarus 159, 369–395.

Kochetova, O.M., 2003. Application of new criteria for selecting perturbed minor planets for determination of masses of perturbing minor planets by dynamical method. In: Reports of Inst. of Applied Astronomy of Russian Acad. Sci. No. 165, St. Petersburg, 42 pp. (in Russian).

Krot, A.N., Meibom, A., Weisberg, M.K., Keil, K., 2002. The CR chondrite clan: Implications for early Solar System processes. Meteorit. Planet. Sci. 37, 1451–1490.

Lagerkvist, C.I., Belskaya, I., Erickson, A., Schevchenko, V., Mottola, S., Chiorny, V., Magnusson, P., Nathues, A., Piironen, J., 1998. Physical studies of asteroids. XXXIII. The spin rate of M-type asteroids. Astron. Astrophys. Suppl. 131, 55–62.

Lupishko, D., 2006. On the bulk density and porosity of the M-type asteroid 16 Psyche. Solar Syst. Res. 40, 214–218.

Magri, C., Ostro, S.J., Rosema, K.D., Thomas, M.L., Mitchell, D.L., Campbell, D.B., Chandler, J.F., Shapiro, I.I., Giorgini, J.D., Yeomans, D.K., 1999. Main-belt asteroids: Results of Arecibo and Goldstone observations of 37 objects during 1980–1995. Icarus 140, 379–407.

Magri, C., Consolmagno, G.J., Ostro, S.J., Benner, L.A.M., Beeney, B.R., 2001. Radar constraints on asteroid regolith properties using 433 Eros as ground truth. Meteorit. Planet. Sci. 36, 1697–1709.

Magri, C., Nolan, M.C., Ostro, S.J., Giorgini, J.D., 2007a. A radar survey of main-belt asteroids: Arecibo observations of 55 object during 1999–2003. Icarus 186, 126–151.

Magri, C., Ostro, S.J., Dcheeres, D.J., Nolan, M.C., Giorgini, J.D., Benner, L.A.M., Margot, J.L., 2007b. Radar observations and a physical model of Asteroid 1580 Betulia. Icarus 186, 152–177.

Margot, J.-L., Brown, M.E., 2003. A low-density M-type asteroid in the main-belt. Science 300, 1939–1942.

Mitchell, D.L., Ostro, S.J., Hudson, R.S., Rosema, K.D., Campbell, D.B., Velez, R., Chandler, J.F., Shapiro, I.I., Giorgini, J.D., Yeomans, D.K., 1996. Radar observations of Asteroids 1 Ceres, 2 Pallas, and 4 Vesta. Icarus 124, 113–133.

Mueller, M., Harris, A.W., Delbo, M., MIRSI team, 2005. 21 Lutetia and other M-types: Their sizes, albedos, and thermal properties from IRTF measurements. Bull. Am. Astron. Soc. 37. Abstract 7.02.

Nedelcu, A., Birlan, M., Vernazza, P., Barucci, A., Fulchignoni, M., Binzel, R.P., 2006. Ground based science of 21 Lutetia. Bull. Am. Astron. Soc. 38. Abstract 59.06.

Nolan, M.C., Harmon, J.K., Hine, A.A., Campbell, D.B., Perillat, P.J., Black, G., Daubar, I.J., Ostro, S.J., Benner, L.A.M., Jurgens, R.F., Slade, M.A., Giorgini, J.D., Chandler, J.F., 1998. First results from the Arecibo Observatory Planetary Radar. Bull. Am. Astron. Soc. 30. Abstract 1036.

Ockert-Bell, M.E., Clark, B.E., Shepard, M.K., Rivkin, A.S., Binzel, R.P., Thomas, C.A., DeMeo, F.E., Bus, S.J., Shah, S., 2008. Observations of X/M asteroids across multiple wavelengths. Icarus 195 (1), 206–219.

Ostro, S.J., Campbell, D.B., Shapiro, I.I., 1985. Mainbelt asteroids: Dual polarization radar observations. Science 229, 442–446.

Ostro, S.J., Hudson, R.S., Nolan, M.C., Margot, J.-L., Scheeres, D.J., Campbell, D.B., Magri, C., Giorgini, J.D., Yeomans, D.K., 2000. Radar observations of Asteroid 216 Kleopatra. Science 288, 836–839.

Pravec, P., Harris, A.W., 2007. Binary asteroid population. 1. Angular momentum content. Icarus 190, 250–259.

Rivkin, A.S., Howell, E.S., Britt, D.T., Lebofsky, L.A., Nolan, M.C., Branston, D.D., 1995. 3-μm spectrophotometric survey of M- and E-class asteroids. Icarus 117, 90–100.

Rivkin, A.S., Howell, E.S., Lebofsky, L.A., Clark, B.E., Britt, D.T., 2000. The nature of M-class asteroids from 3-μm observations. Icarus 145, 351–368.

Sada, P.V., Warner, B.D., 2007. Rotation period of Asteroid 340 Eduarda and refined period for Asteroid 71 Niobe. Minor Planet Bull. 34, 37–38.

Shepard, M.K., Kressler, K.M., Clark, B.E., Ockert-Bell, M.E., Nolan, M.C., Howell, E.S., Magri, C., Giorgini, J.D., Benner, L.A.M., Ostro, S.J., 2008. Radar observations of E-class Asteroids 44 Nysa and 434 Hungaria. Icarus, doi:10.1016/j.icarus.2007.12.018, in press.

Shevchenko, V.G., Tedesco, E.F., 2006. Asteroid albedos deduced from stellar occultations. Icarus 184, 211–220.

Simpson, R.A., 1976. Proc. IEEE Trans. Antennas Propag. AP-24, 17.

Tedesco, E.F., Noah, P.V., Noah, M., 2002. The supplemental IRAS minor planet survey. Astron. J. 123, 1056–1085.

Tholen, D., 1984. Asteroid taxonomy from cluster analysis of photometry. Ph.D. thesis, Univ. of Arizona, Tucson. 150 pp.

Torppa, J., Kaasalainen, M., Michalowski, T., Kwiatkowski, T., Kryszczynska, A., Denchev, P., Kowalski, R., 2003. Shapes and rotational properties of thirty asteroids from photometric data. Icarus 164, 346–383.

Tiuri, M.E., 1964. Radio astronomy receivers. IEEE Trans. Antennas Propag. AP-12, 930–938.

Tungalag, N., Shevchenko, V.G., Lupishko, D.F., 2002. Rotation parameters and shapes of 15 asteroids. Kinem. Phys. Celest. Bodies 18, 358–364.

Viateau, B., 2000. Mass and density of Asteroids (16) Psyche and (121) Hermione. Astron. Astrophys. 354, 725–731.

Vilas, F., 1994. A cheaper, faster, better way to detect water of hydration on Solar System bodies. Icarus 111, 456–467.

Warner, B.D., 2006. Asteroid lightcurve analysis at the Palmer Divide Observatory—Late 2005 and early 2006. Minor Planet Bull. 33, 58–59.

Warner, B.D., Shepard, M.K., Harris, A.W., Pravec, P., Crawford, G., Husarik, M., 2006. Analysis of the lightcurve of 71 Niobe. Minor Planet Bull. 33, 102–103.

Warner, B.D., Behrend, R., Poncy, R., Coliac, J.-F., 2008. Lightcurve analysis of 758 Mancunia. Minor Planet Bull. 35, 25.

Wasserman, L.H., Millis, R.L., Franz, O.G., 1986. The occultation of AG + $20^\circ 1138''$-by 129 Antigone on 11 April 1985. Bull. Am. Astron. Soc. 18. Abstract 797.

Weidenschilling, S.J., Chapman, C.R., Davis, D.R., Greenberg, R., Levy, D.H., Binzel, R.P., Vail, S.M., Magee, M., Spaute, D., 1990. Photometric geodesy of main-belt asteroids. III. Additional lightcurves. Icarus 86, 402–447.

Zappala, V., Knezevic, Z., 1984. Rotation axes of asteroids: Results for 14 objects. Icarus 59, 436–455.

Zellner, B., Leake, M., Morrison, D., Williams, J.G., 1977. The E-asteroids and the origin of the enstatite achondrites. Geochim. Cosmochim. Acta 41, 1759–1767.

Zolensky, M., McSween Jr., H.Y., 1988. Aqueous alteration. In: Kerridge, J.F., Matthews, M.S. (Eds.), Meteorites and the Early Solar System. Univ. of Arizona Press, Tucson, pp. 114–143.